Drift og vedlikehold
Fagressurs Drift og vedlikehold
Geofag Drift og vedlikehold
7.1.2025

Statens vegvesen

Snowpack mapping with georadar (GPR) on UAS

Quantitative analysis of GPR data for snowpack properties

STATENS VEGVESENS RAPPORTER Nr. 1025

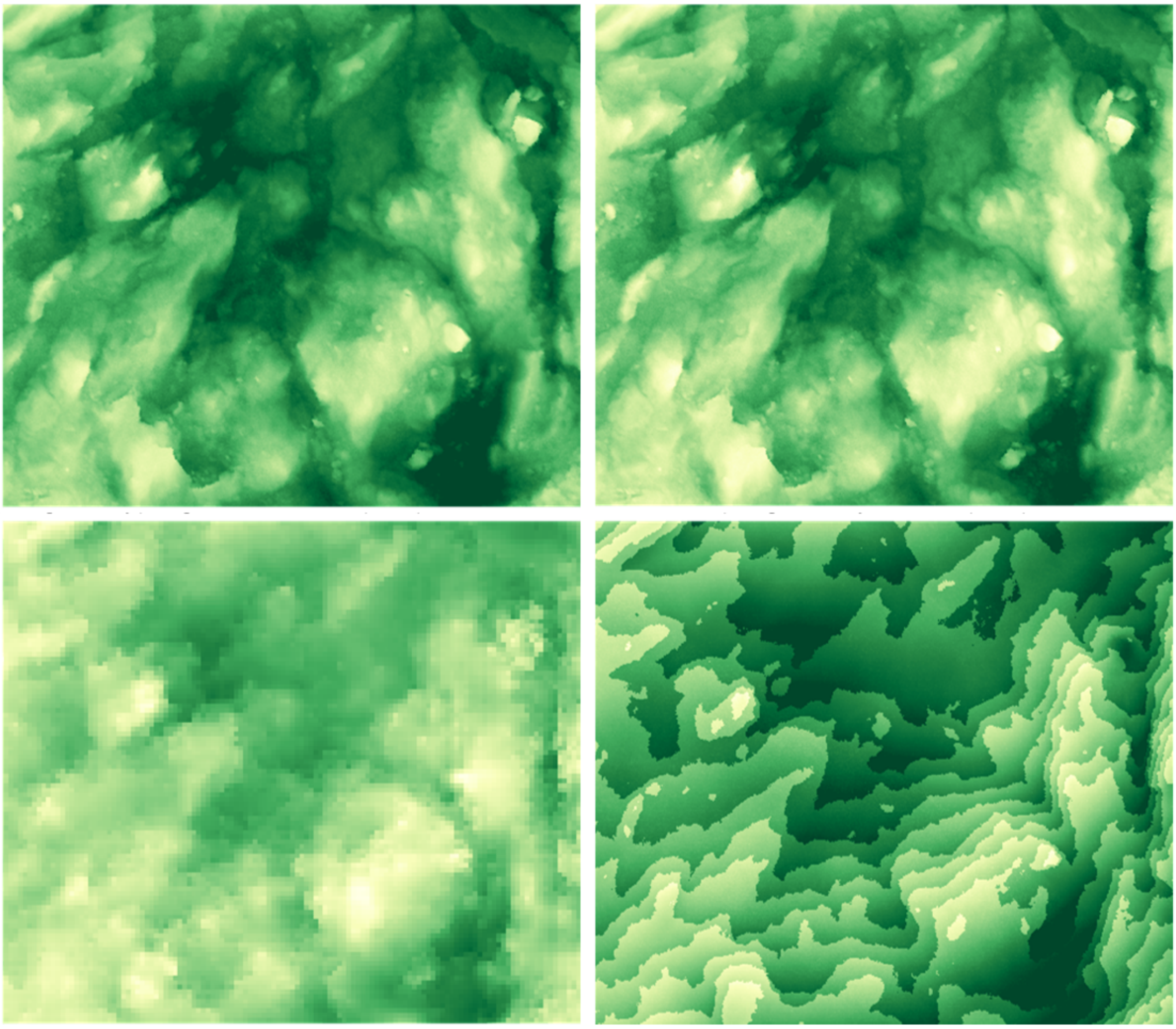

Illustration: GEOSFAIR project

Statens vegvesens rapporter

NPRA reports
Norwegian Public Roads Administration

Tittel
Snowpack mapping with georadar (GPR) on UAS

Undertittel
Quantitative analysis of GPR data for snowpack properties

Forfatter
Martin Châtel and others (find complete author list on page 3)

Avdeling
Fagressurs Drift og vedlikehold

Seksjon
Geofag Drift og vedlikehold

Prosjektnummer
C15115

Rapportnummer
1025

Prosjektleder
Tore Humstad

Godkjent av
Viggo Aronsen

Emneord
avalanches, snow, GPR, georadar, GEOSFAIR

Sammendrag
I prosjektet GEOSFAIR (2021-2024) er det utviklet metoder for å utlede kvantitativ informasjon om snødekket fra GPR-data samlet inn med drone. En automatisk algoritme ble tatt i bruk for å finne snøoverflate og overgang mellom snø og bakke. Ved å bruke et tett datasett med GPR-linjer hver 50 cm ble tiden signalene brukte gjennom snøen konvertert til snøhøyder, Dette ble sammenlignet med dronebaserte LiDAR-undersøkelser og snøprofiler. I tillegg ble en maskinlæringsalgoritme testet for å utlede snøtetthet fra GPR-data. Dette viste lovende data ved testing på reelle målinger fra 2022-2024.

Antall sider 51

Title
Snowpack mapping with georadar (GPR) on UAS

Subtitle
Quantitative analysis of GPR data for snowpack properties

Author
Martin Châtel and others (find complete author list on page 3)

Department
O&M Planning and Engineering Services

Section
Geomechanics

Project number
C15115

Report number
1025

Project manager
Tore Humstad

Approved by
Viggo Aronsen

Key words
snøskred, GPR, georadar, naturfarer, GEOSFAIR

Summary
As part of the GEOSFAIR project (2021-2024), methods were developed to derive quantitative snowpack information from GPR data captured by UAS. An automatic picking algorithm was implemented to identify snow surface and snow-ground interfaces. Using a dense dataset with GPR lines every 50 cm recorded at Fonnbu in March 2024, travel times were converted to snow heights and compared with UAS-based LiDAR survey results. Different bare ground models were used for LiDAR snow heights. Additionally, a machine learning algorithm was tested to derive snow density from UAS GPR data, showing promising results when tested on real data from 2022-2024.

Pages 51

Snowpack mapping with georadar (GPR) on UAS

Quantitative analysis of GPR data for snowpack properties

Authors:

Martin Châtel, Bastien Dupuy, Madeline Lee, Arnt Grøver (SINTEF), Sean Salazar, Regula Frauenfelder (NGI), Halgeir Dahle and Tore Humstad (NPRA)

Published on January 7th, 2025, as a part of the GOESFAIR project, as deliverable D2.3 Sensor data interpretation (machine learning-based software)

Content

Abstract 5

1 INTRODUCTION 6

APPENDIX: Geophysical snow-mapping using Ground Penetrating Radar (GPR) borne by Uncrewed Aerial Vehicles (UAVs) (Martin Châtel, 2024) i

Abstract

We present methods to derive quantitative snowpack information from GPR (Ground Penetrating Radar, in Norway often called 'georadar') data captured by UAS (Uncrewed Aerial System). After conventional data processing, we implemented and successfully tested an automatic picking algorithm that allows to identify and select snow surface and snow-ground interfaces automatically. Using an extensive spatially dense dataset (GPR lines every 50 cm) recorded at Fonnbu in Mars 2024, we apply this automatic picking algorithm and automatically determine the travel times between snow surface and snow-ground interface for the full area of interest. Using a density log derived in a neighbouring snowpit, we convert these travel times into snow heights. We test different spatial interpolation algorithms to derive snow height maps at different resolution and we compare these with snow height derived from an UAS-based LiDAR survey carried out on the same day. To calculate LiDAR (Light Detection and Ranging) snow heights, we used different bare ground models, including the national airborne LiDAR model (from høydedata.no), UAS photogrammetry and UAS LiDAR surveys carried out in October 2024.

The second part of this quantification work consists in testing a machine learning algorithm to derive snow density directly from the UAS GPR data. We use a wave propagation modelling tool to generate an extensive dataset of synthetic UAS GPR data representing the variability of expected data for a variety of dry snowpacks. We use this synthetic dataset to train successfully a convolutional neural network. Testing the training on real UAS GPR data recorded at Fonnbu in March 2023 and 2024 and at Storlidalen in March 2022 is promising and allows to recover snow density profiles which are consistent with observations from snowpits.

1 INTRODUCTION

This report is mostly based on the master thesis by Martin Châtel (given in Appendix), master student at the École Polytechnique (Palaiseau, France) who has been carrying out his master internship at SINTEF during spring and summer 2024. Martin has been developing the automatic picking algorithms, deriving snow height maps and implementing the machine learning approach to derive snow density profiles.

To complement his extensive work, we have been updating the snow height comparisons with newly recorded data in October 2024. Previous work compares the snow height map from UAS GPR data with the snow height map from UAS LiDAR survey using a bare ground model from the national airborne LiDAR model (from høydedata.no), see Figure 1. This bare ground model limits the spatial resolution, and comparisons were only possible using a Kriging interpolation with low spatial resolution. Despite this lack of resolution, Figure 2 still shows good agreement between the derived snow heights, even though a systematic underestimation of snow height is observed in the GPR data, likely due to some errors during automatic picking.

New surveys, both UAS LiDAR and UAS photogrammetry, were carried out in October 2024 by the Norwegian Geotechnical Institute (NGI) to derive a high-resolution bare ground model. The derived snow heights are given in Figure 3. Three different snow height models are calculated accounting for different bare ground models, where the snow height is calculated by subtracting the DEM (Digital Elevation Model) with snow cover from the DEM without snow. Overall, we observe that the snow height model using UAS LiDAR bare ground give the best resolution, similar for both interpolation sizes (5 and 25 cm).

We then plot the differences between UAS GPR and UAS LiDAR snow heights for these three models (Figure 4). When comparing with the best resolution LiDAR model, we observe that the differences between the two snow height models are rather small and limited to specific areas. When we highlight these areas of larger differences (both positive and negative) in Figure 5, we see that most of the large differences' areas are linked to strong topography features, such as large rock boulders and small branches of the creek. We think that this can be related to the fact that UAS GPR will be able to catch these small steep topography features while the DEM produced by the UAS LiDAR will have difficulty to map them. On the other hand, as we consider un-migrated GPR data for the picking of the snow-ground interfaces – due to a lack of relevant EM (ElectroMagnetic) velocity model – some of these steep features are likely not located correctly and/or with incorrect slopes in the GPR data. More details on the automatic picking methods, the spatial interpolation algorithm and the estimations of errors are given in the MSc thesis of Martin Châtel (Appendix).

Overall, we confirm that UAS GPR data contains a lot of relevant information allowing the quantification of snow height and snowpack properties (i.e. density). Snow height mapping from GPR data shows to be possibly better than snow height mapping from LiDAR at mapping small ground features; a fact which can be crucial for local avalanche forecasting and identification of trigger points (shallower snowpack around boulders). The quantification of snow density using machine learning is promising and will benefit from further research to be validated and extended to wet snowpacks. It is important to keep in mind that the ability to resolve thin layers, whether in the GPR image or in the snow density model, will always be limited by the antenna frequency. With the 1 GHz broadband antenna used in this work, in a 300 kg/m3 dense snow, the vertical resolution will be between 3 and 10 cm. In addition to their thickness, the resolution and identification of thin layers also strongly depends on the density contrast between them. Usually, a dense melt-freeze crust on top or bottom of low density snow will be possible to identify even if very thin.

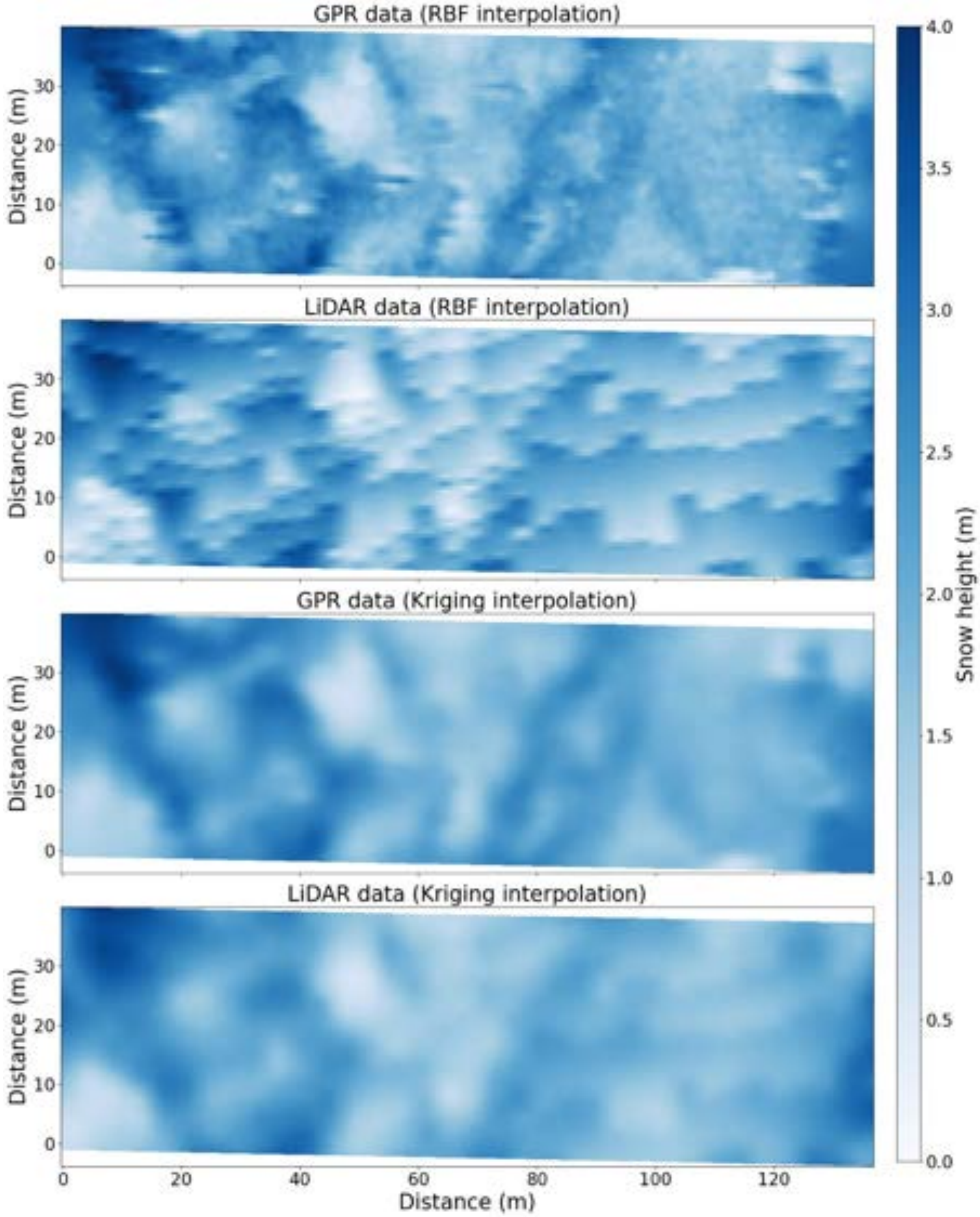

Figure 1: Snow height maps from GPR and LiDAR data using RBF and Kriging interpolations. The UAS GPR snow height is calculated by down-sampling the GPR data (1 m resolution) and using a constant average EM wave velocity estimated from the nearby snowpit density log. The UAS LiDAR snow height is calculated by subtracting the DEM surveyed with UAS LiDAR in March 2024 (with snow cover) with the bare ground model of the national airborne LiDAR model. The maps are oriented to the North.

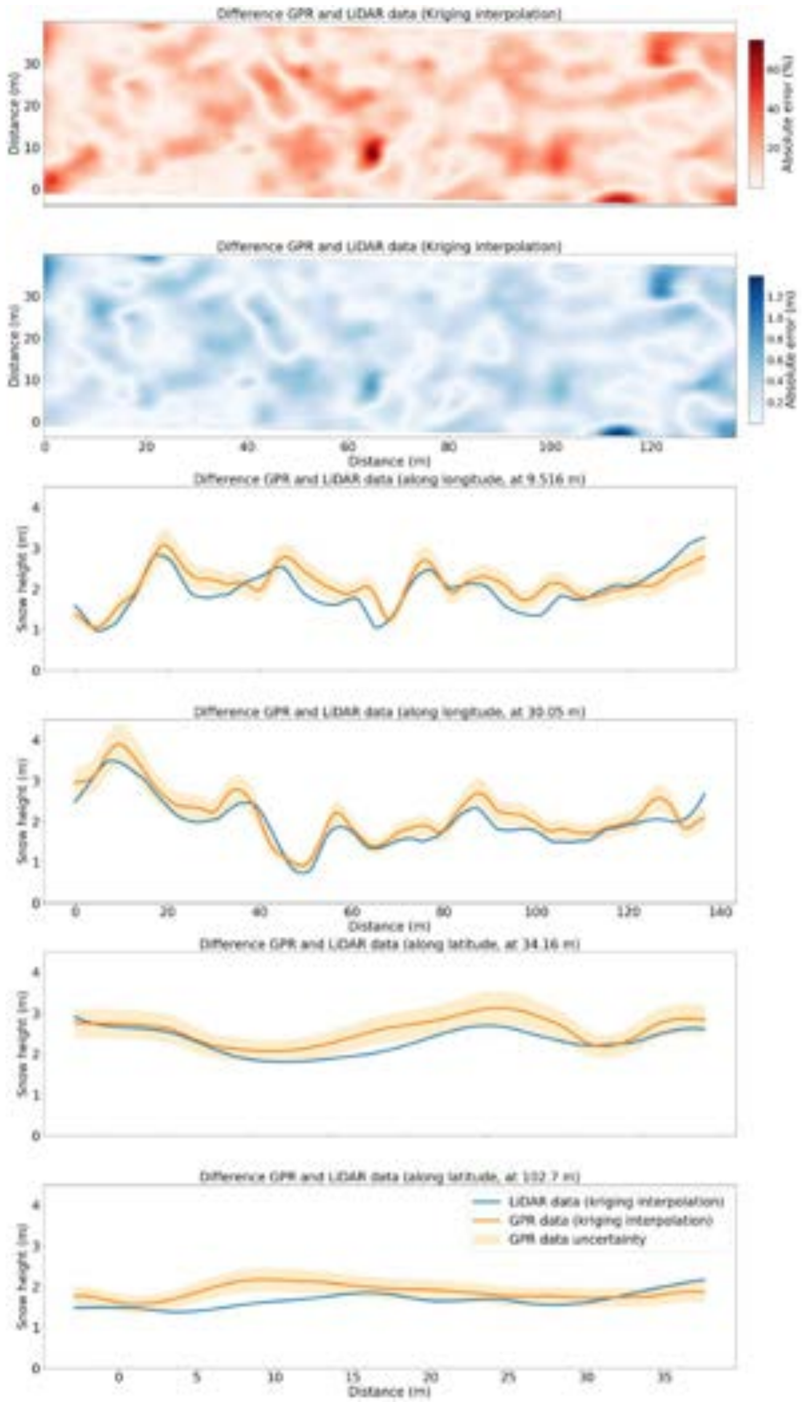

Figure 2: Comparison of UAS GPR and UAS LiDAR (with the national airborne LiDAR bare ground model) snow heights. From top to bottom: absolute error in %, absolute error in meters, longitudinal cross section at 9.516 m, longitudinal cross section at 30.05 m, latitudinal cross section at 34.16 m, latitudinal cross section at 102.7 m. The orange and blue lines stand for the snow height from UAS GPR and UAS LiDAR (with the national airborne LiDAR bare ground model), respectively. The orange shading gives an estimate of the GPR snow height uncertainty related to the uncertainty in snow density estimates in the snowpit (which affects the average EM velocity used to convert GPR data from time to depth).

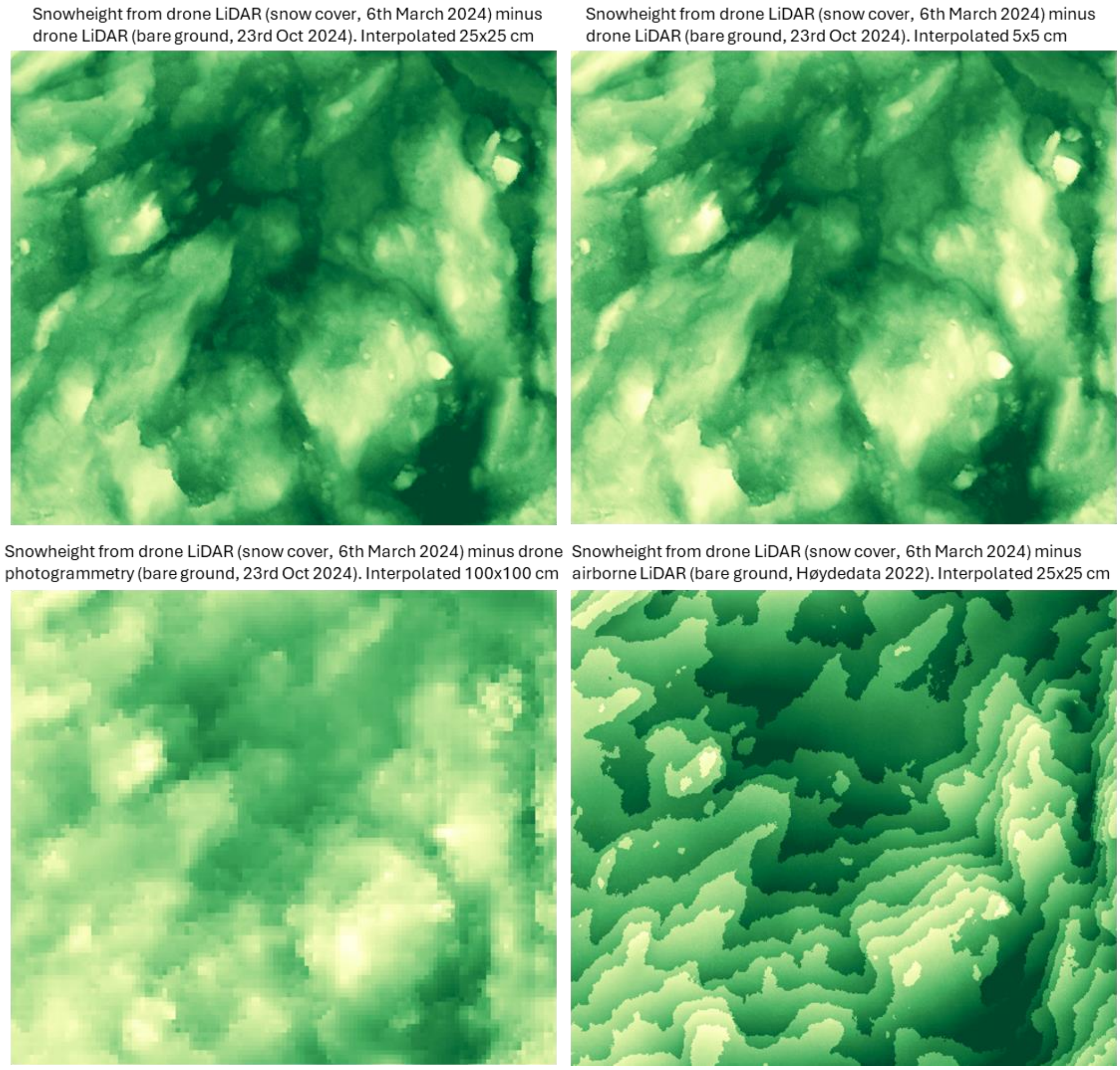

Figure 3: Different snow height models calculated for the UAS LiDAR survey of 6th March 2024. The bare ground model used to subtract the DEM with snow cover is either an UAS LiDAR survey, interpolated on 25x25 cm grid (top left), on 5x5 cm grid (top right), an UAS photogrammetry DEM on a 1x1 m grid (bottom right) or the national airborne LiDAR bare ground model (bottom right).

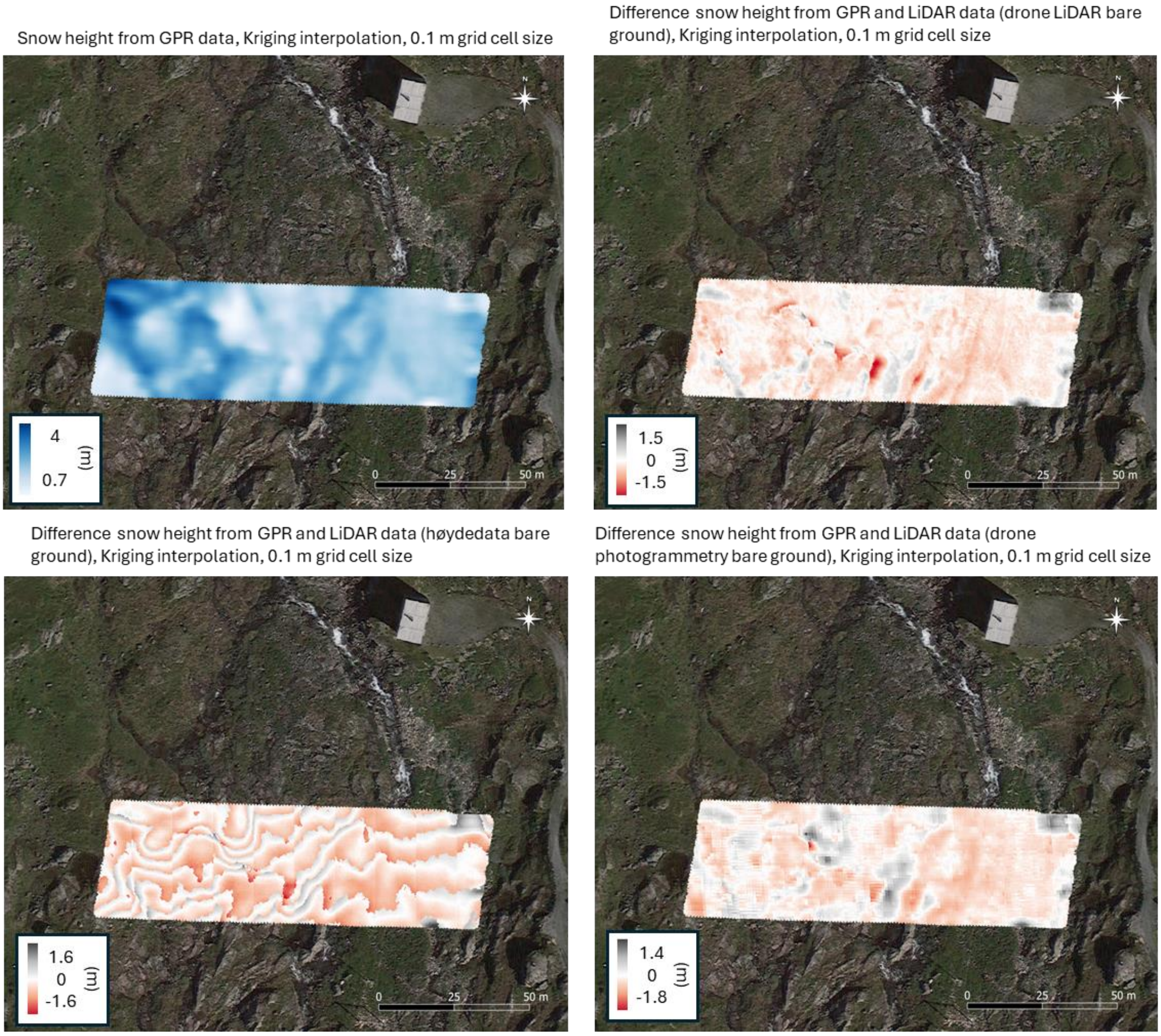

Figure 4: Snow height from UAS GPR data (top left). Differences between GPR snow height and LiDAR snow height with different bare ground DEM (Figure 3): UAS LiDAR bare ground (top right), the national airborne LiDAR bare ground model (bottom left), UAS photogrammetry bare ground (bottom right).

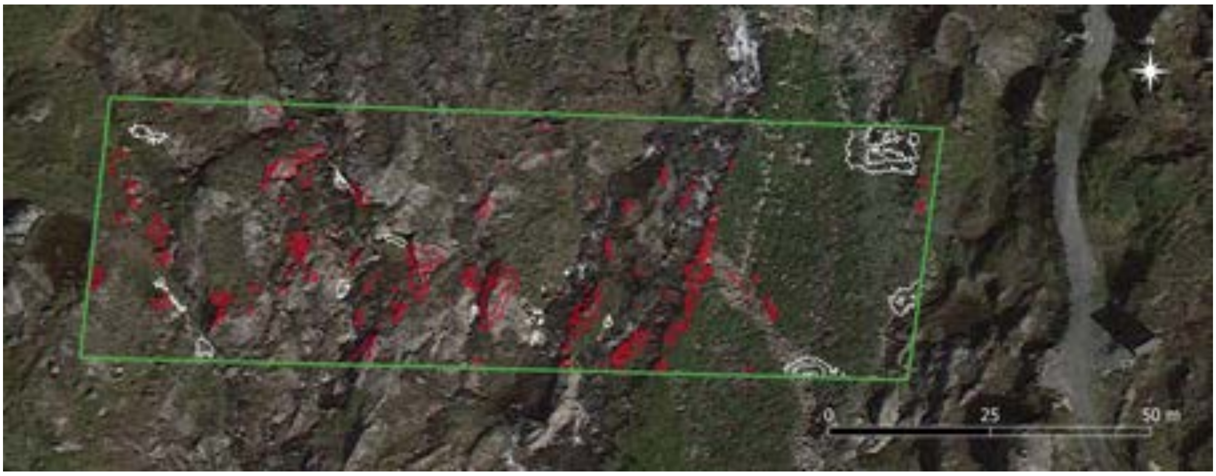

Figure 5: Highlights of main differences between snow height maps from UAS GPR and from UAS LiDAR (with UAS LiDAR bare ground). Positive and negative differences in white and red, respectively.

APPENDIX: Geophysical snow-mapping using Ground Penetrating Radar (GPR) borne by Uncrewed Aerial Vehicles (UAVs) (Martin Châtel, 2024)

Martin Châtel (2024): Geophysical snow-mapping using Ground Penetrating Radar (GPR) borne by Uncrewed Aerial Vehicles (UAVs).

Internship report (Master thesis), April 8th – July 26th, 2024,

INTERNSHIP REPORT

Geophysical snow-mapping using Ground Penetrating Radar (GPR) borne by Uncrewed Aerial Vehicles (UAVs).

April 8th - July 26th, 2024

Martin Châtel

ABSTRACT

Unmanned Aerial Vehicle-borne (UAV-borne) geophysics and remote sensing are increasingly utilized for monitoring the cryosphere. Snow cover measurements benefit greatly from airborne remote sensing and geophysical data due to their extensive coverage, efficiency, non-destructive nature, and safety. Ground Penetrating Radar (GPR) is particularly effective for snow measurements as it relies on electromagnetic wave propagation, which is sensitive to snow properties. For example, in dry snow, the propagation velocity is directly affected by the density variations in the snow layers. Consequently, the electromagnetic (EM) energy emitted by the GPR sensor is divided into reflected and transmitted waves at each interface where snow density changes, including the snow surface and the snow-bedrock interfaces.

This capability makes GPR suitable for applications such as snow height mapping, glacier mass balance assessment, and snow avalanche hazard analysis. These applications form the core motivation behind the GeoDrones project, which aims to derive large-scale snowpack information.

Achieving these objectives presents two major challenges: developing an algorithm that can automatically identify the snowpack structure on a large-scale, and deriving the electromagnetic (EM) velocity profile within the snowpack from signal amplititudes. The first challenge can be addressed by detecting the major reflections from signal amplitudes variation, which correspond to the air-snow and snow-rock interfaces. The second challenge is more complex and was tackled by employing a Convolutional Neural Network (CNN) trained to predict a velocity profile from a given signal trace.

This study leveraged a comprehensive range of GPR surveys, using 400 MHz and 1 GHz antennas, conducted in various locations (Jufvonne, Storlidalen, and Fonnbu) between 2022 and 2024.

To summarize our results, we can first highlight that the picking algorithm successfully identified the snow surface and the snow-rock interface with an error of less than 10%. We observed better accuracy on grassy or icy slopes than on heterogeneous rocky terrain. Subsequently, snow height estimates were obtained for a 40×130m area and compared with low-resolution LiDAR data. Notably, there was a good agreement between the two surveys, despite a 6% overestimation, likely attributable to either the automatic picking process or the reference data. Furthermore, the machine learning algorithm effectively retrieved velocity profiles that were consistent with LiDAR observations, exhibiting an absolute error of 5% and showing reliable results for the detection of fine layers.

RÉSUMÉ

La géophysique et la télédétection aéroportée par drone sont de plus en plus utilisées pour surveiller la cryosphère. Les mesures de la couverture neigeuse bénéficient grandement de la télédétection aéroportée et des données géophysiques en raison de leur capacité de couverture , de leur efficacité, de leur nature non destructive et de leur fiabilité. Le radar à pénétration de sol (GPR) est particulièrement efficace pour les mesures de neige car il repose sur la propagation des ondes électromagnétiques, sensibles aux propriétés de la neige. Par exemple, dans la neige sèche, la vitesse de propagation est directement influencée par les variations de densité dans les couches de neige. En conséquence, l'énergie électromagnétique (EM) générée par le capteur GPR est partitionnée (réfléchie et transmise) à chaque interface où la densité de la neige change, ainsi qu'à l'interface entre la neige et le sol.

Cette capacité rend le GPR adapté à des applications telles que la cartographie de la hauteur de neige, l'évaluation du bilan de masse des glaciers et l'analyse des risques d'avalanches. Ces applications constituent la motivation principale du projet GeoDrones, qui vise à dériver des informations sur le manteau neigeux à grande échelle.

Atteindre ces objectifs présente deux défis majeurs : développer un algorithme capable d'identifier automatiquement la structure du manteau neigeux à grande échelle, et déduire le profil de vitesse électromagnétique (EM) au sein du manteau neigeux à partir des traces de signal. Le premier défi peut être abordé en détectant les principales réflexions à partir des variations d'amplitude du signal, correspondant aux interfaces air-neige et neige-roche. Le deuxième défi est plus complexe et a été traité en utilisant un réseau de neurones convolutionnels (CNN) entraîné à prédire un profil de vitesse à partir d'une trace de signal donnée.

Cette étude a utilisé une gamme large de relevés GPR, avec des antennes de 400 MHz et 1 GHz, réalisés dans divers endroits (Jufvonne, Storlidalen et Fonnbu) entre 2022 et 2024.

Pour résumer nos résultats, nous pouvons d'abord souligner que l'algorithme de sélection a identifié avec succès la surface de la neige et l'interface neige-roche avec une erreur de moins de 10 %. Nous avons observé par ailleurs une meilleure précision sur les pentes herbeuses ou glacées que sur les terrains rocheux hétérogènes. Par la suite, des estimations de hauteur de neige ont été obtenues pour une zone de 40×130 m et comparées aux données LiDAR à basse résolution. Il y avait notamment une bonne concordance entre les deux relevés, malgré une surestimation de 6 %, probablement due au processus de sélection automatique ou aux données de référence. En outre, l'algorithme de machine learning a récupéré efficacement les profils de vitesse qui étaient cohérents avec les observations LiDAR, avec une erreur absolue de 5 %, et a montré des résultats fiables pour les couches fines.

AKNOWLEDGEMENT

I would like to express my deepest gratitude to Bastien Dupuy, my supervisor and leader of the GeoDrones project, for placing his confidence in me and introducing me to the fields of signal physics, data science, and snow science physics. I also appreciate the time he consistently dedicated to clarifying and discussing complex concepts.

I must also extend my sincere thanks to Arnt Grøver, whose office was conveniently located next to mine. He was almost always available to assist me with coding errors and software installations. Additionally, I am grateful to Madeline Lee, Dias Urozayev, and all members of the geophysics group who welcomed and supported me during this internship.

A special thanks goes to Anthime Jeante and Baptiste Hermet, fellow interns at SINTEF, whose positive attitudes and insightful remarks brightened my daily life.

CONTENTS

1 Introduction **6**
1.1 Presentation of the Geodrones and Geosfair project 6
1.2 My Role in the Project 7
1.3 Litterature Review 9

2 Methodology **10**
2.1 UAV and GPR Hardware Configuration 10
2.2 Data Pre-Processing Workflow 11
2.3 Algorithm Development and Implementation 13
2.3.1 Fundamentals of GPR Wave Propagation 13
2.3.2 Description of the Automatic Picking Algorithm 15

3 Testing and results **17**
3.1 Field Site Description 17
3.2 Validation Methods 18
3.2.1 Validation Method for Automatic-Picking 18
3.2.2 Validation Method for CNN Velocity Prediction 21
3.3 Results 24
3.3.1 Snow Depth Large Scale Results 24
3.3.2 GPRNet Results 29

4 Conclusion and further work **31**

- 1 -
INTRODUCTION

1.1 Presentation of the Geodrones and Geosfair project

Norway's mountainous terrain and remote locations make its road and train infrastructure crucial but also highly susceptible to natural hazards, particularly snow avalanches. Additionally, the country's topography and climate render it prone to other natural hazards such as landslides, rockfalls, and floods. With rising temperatures and changing precipitation patterns, these hazards are expected to worsen, increasing the vulnerability of Arctic regions and Norway as a whole. Consequently, monitoring spatiotemporal changes in snow cover has become critically important, even extending beyond the Arctic regions.

Snow height, defined as the vertical distance from the base to the snowpack surface, is essential for estimating glacier mass balance and forecasting geohazards such as avalanches. One can also derive the snow height and snow density profile to obtain the Snow Water Equivalent (SWE) which is crucial for preventing floods, debris flows and even for supporting the hydropower industry (which produces the major part of electricity in Norway). On the other hand, understanding the layering and density variations within the snowpack is vital for avalanche forecasting, especially for slab avalanches, where stability depends on the density contrasts and snow grain sizes, such as a high-density slab layer atop a low-density weak layer.

To optimize spatial coverage, resolution, and data quality, the Geodrones project proposes using Unmanned Aerial Vehicle-borne (UAV-borne) Ground Penetrating Radar (GPR) systems to derive large-scale snowpack information. The project aims to map and monitor natural hazards using multipurpose UAVs, focusing on building an autonomous geo-drone platform and developing innovative real-time data processing and analysis approaches to support decision-making. The first demonstration of UAV-borne GPR reliability is focused on snow and ice because GPR has a good penetration in it. But the results could outpass this domain and have application in archeology for example. Indeed, the Geodrones project, which is a Strategic Internal Project (SIP) funded by SINTEF, not only focuses on snow mapping but more broadly aims to develop drone expertise applied to geoscience, with a budget of 14 MNOK (1.2 MEUR).

This project is also supported by the GeoSFAir (Geohazard Survey From Air) initiative, funded by the research council of Norway and by Statens vegvesen, the Norwegian Public Road Administration(NPRA), in collaboration with SINTEF and the Norwegian Geotechnical Institute (NGI). Currently, Statens Vegvesen relies on visual observation, hand-dug snow pits, stationary sensors, and weather station data to make decisions regarding road closures and re-openings. Therefore, the project aims to enhance remote information collection using sensors-equipped drones, reducing the risks to employees and reaching inaccessible areas. A schematic representation of the drone flight, shown in Figure 1, demonstrates its capability for autonomous operation in sloping terrain, enabling both surface and subsurface mapping. This interdisciplinary project combine snow science, geotechnics, geophysics, remote sensing, drone

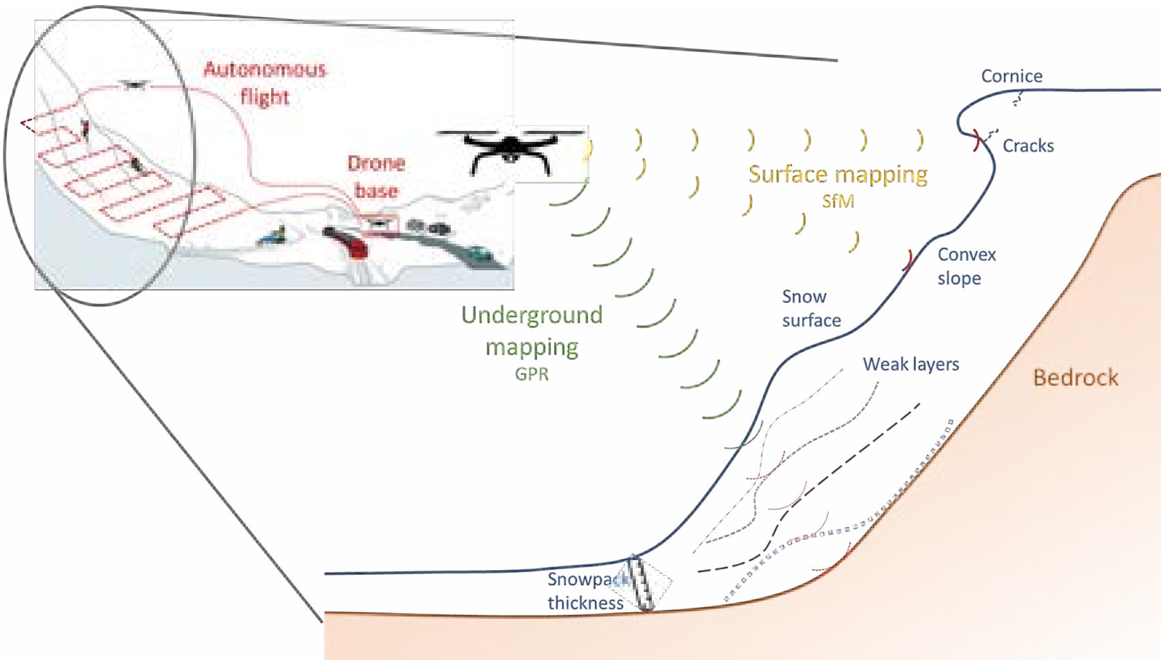

Figure 1: Schematic representation of the drone flight (SFM means Structure from motion and is a photogrammetric range imaging technique for estimate surface shape), credit Sintef Industri

and robotics, and decision making studies. Spanning from 2021 to 2024, it has a total funding of 11.9 MNOK(1.1 MEUR) (with 3.1 MNOK allocated to SINTEF).

The GeoSFAir project is divided into four scientific work packages (WPs). The first two WPs, led by SINTEF, focus on hardware (aircraft platforms and sensors) and software (mission planning, automation, and processing workflow). WP3, managed by NGI, is dedicated to field demonstrations and interpretation of results. Finally, WP4, led by NPRA, will integrate the outcomes of WP1, WP2, and WP3 to enhance decision support.

1.2 My Role in the Project

To achieve snow height mapping, glacier mass balance estimation, and snow avalanche hazard assessment, a primary challenge is to derive snow height from the two-way travel time of waves. This internship is structured to address this issue through three primary objectives: automating the picking of main horizons, the application of this method to perform a 2D mapping of snow height and the derivation of the EM velocity via a neural network training. Specifically, my mission is to develop algorithms that will be integrated into a larger, already well-advanced processing workflow which has been implemented by Arnt Grøver. The goal of this processing is to transform the GPR raw data (see Figure 2b) into either a snow height map (see Figure 2c) or, even, a snow layer map(see Figure 18). In Figure 2, a raw signal trace and its associated raw profile are displayed, representing the juxtaposition of 930 traces recorded at

5 cm intervals during the drone flight. Even if we can see the snow-ground interface (around 50 ns of travel time in the middle of the profile) it is harder to visualize air-snow interface (around 25 ns) and it is evident that raw profiles require preprocessing to enhance their readability. Subsequently, snow height must be extracted from these profiles to facilitate large-area snow height mapping. If the pre-processing workflow has already been implemented(cf:2.2 Data Pre-Processing Workflow) the second phase will be the main focus of my internship. Essencially, the program will be implemented in a GPR data processing app that can be automatized to be used by non-geophysicists. The final aim for them is to be autonomous for using the drone especially in the interpretation of the GPR data to help them in decision making in the closing of the roads. This part of the project logically falls under WP2 (mission planning, automation, and processing workflow), led by Bastien Dupuy, my supervisor. To achieve my mission, I can count on the help of my colleagues and particularly Bastien Dupuy and Arnt Grøver.

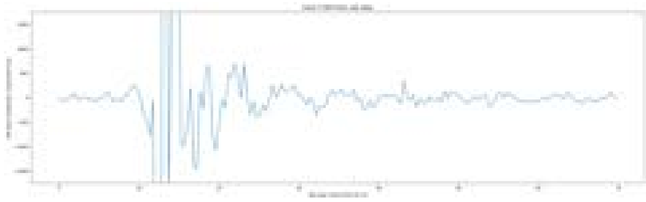

(a) Trace n°400 recorded by the drone

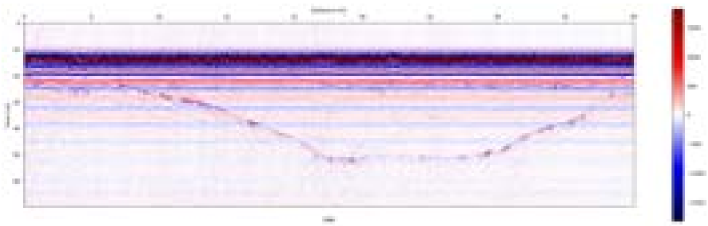

(b) Trace juxtaposition forming the raw profile

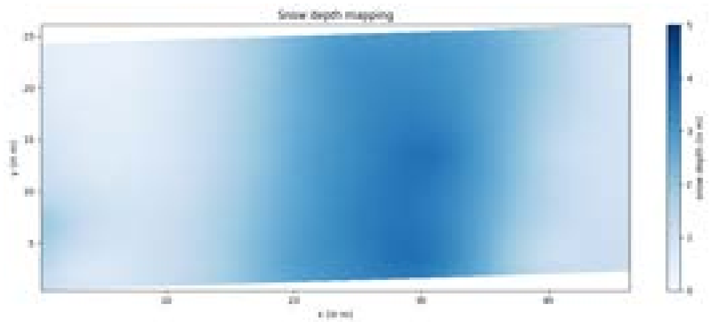

(c) Snow depth mapping interpolated from 3 segments spaced by 10m each

Figure 2: (a) amplitude of a raw signal trace (b) Raw GPR profile where the traces of the signal recorded every 5cm of the drone flight and combined in a profile which shows the intensity of the received signal in µV (c) Snow depth mapping derived with the information contained in 3 raw profiles spaced by 10m

1.3 Litterature Review

GPR has proven to be effective in snow mapping. Di Paolo et al. [1] demonstrated that GPR can derive estimates of snow properties, snow density, and Snow Water Equivalent (SWE), which correlate well with time-domain reflectometry (TDR) measurements. Similarly, Godio et al. [2] validated an upward-looking GPR with a 1500 MHz antenna, using TDR at a fixed location to derive snow density. Additionally, Griessinger et al. [3] used multioffset ground GPR to derive snow ablation rates for avalanche forecasting. In their work, travel times were calibrated using density profiles to calculate permittivity with empirical relationships, which have proven to be accurate according to Di Paolo et al. [4]. This ultimately allowed for the derivation of snow height variations along the measured sections. Finally, Dupuy et al. [5] shows the relevance of the uses of UAV in GPR snow mapping, by validating the repeatability of UAV-borne GPR data and showing the rapidity of such a method. This study also investigated optimal flight parameters, such as altitude and speed, to maximize Signal-to-Noise Ratio (SNR). Additionally, it emphasized the significance of antenna frequency, noting that higher frequencies yield better resolution but reduced depth penetration. The study also outlined pre-processing techniques to enhance GPR data utilization, including the use of an open-source R library developed by Huber and Hans [6]. Figure 4 illustrates the workflow, showing clear visualization of the air-snow and snow-rock horizons after the sixth step. You will notice that the vertical axis is in time domain since to derive snow height further steps are needed.

First, we need to identify the different layers in the snow profile and then derive permittivity to obtain EM velocity at each point. To streamline the identification of the main horizons, several methods were evaluated: Thresholding, Short-Term-Average/Long-Term-Average (STA/LTA), computer vision, and machine learning algorithms. While the STA/LTA method (Wong et al. [7]) and machine learning algorithms (Mardan [8]) are well-documented in seismic data analysis, their applicability to GPR data, which uses electromagnetic waves, is less clear. Dossi et al. [9] applied computer vision for automated layer picking in GPR data and subsequent Snow Water Equivalent (SWE) inversion for glaciers.

The STA/LTA method, which identifies signal peaks where the short-term average significantly exceeds the long-term average, was found to generate numerous outliers, requiring substantial refinement to be practical. Computer vision techniques showed promise for detecting intricate interfaces within the snowpack but seemed overly complex for identifying main layers. Machine learning algorithms, while potentially powerful, require extensive training data, which was not available, and function as black boxes, complicating interpretability.

Based on a review of the literature and preliminary tests, my supervisor (Dupuy) determined that a basic thresholding algorithm could be effective. I developed this algorithm to identify the first point in each trace where the signal exceeds a predefined threshold. With added features such as automatic outlier removal based on layer continuity, this method proved accurate. It was chosen for its simplicity, speed, and effectiveness, although future exploration of other techniques, such as computer vision for intermediate interfaces, is recommended. To our knowledge, this approach has not previously been referenced in the GPR snow data literature.

In the domain of snow height mapping, a primary challenge is to derive permittivity from signal traces. To avoid this, a first possibility is to use snowpits to obtain permittivity profiles based on density profiles. Extensive literature covers this topic, with Di Paolo et al. [4] providing a comprehensive overview of the empirical and physical relationships linking snow density to permittivity. However, snowpits offer only point measurements, and density profiles can exhibit significant variability according to Machguth et al. [10]. Furthermore, density measurements are not systematically performed in snowpits, and while it is possible to derive snow density based on hardness and grain type, this method has very low precision Kim and Jamieson [11].

Machine learning methods have shown promise in deriving permittivity profiles from signal traces. Leong and Zhu [12] employed an approach that involved generating a synthetic dataset of paired permittivity profiles and associated signal traces, following the methodology of Irving and Knight [13]. They then trained and tested an encoder-decoder based convolutional neural network (CNN) on this synthetic data, where the signal amplitudes are the features and the velocity profile the labels. The CNN utilized the DeepLabV3 architecture, which is known for its accuracy in feature extraction from images. The model's accuracy was subsequently validated on real data.

- 2 - METHODOLOGY

2.1 UAV and GPR Hardware Configuration

Depending on desired penetration and resolution, we utilize two types of GPR systems provided by Radar Systems Inc., mounted on a commercial off-the-shelf quadcopter, the DJI Matrice 300 RTK. The high-frequency system is a shielded bistatic antenna with a theoretical central frequency of 1 GHz and an operating bandwidth of 600-1300 MHz at -6 dB. It is important to also note that, in general, an antenna has a theoretical spatial resolution of $\lambda/10$ (ranging from 3 cm in air to 1.7 cm in ice for a 1 GHz antenna). However, in practice, the resolution is often lower and can even decrease to $\lambda/2$. The transmitter and receiver are separated by 17cm and synchronised. It records 512 samples per trace with a time range to be chosen between 50 and 300 ns, it measures both magnetic and electrical field and gives the amplitude result in µV. With such sampling, 50 traces per second can be recorded and if its flies at a velocity of 2 m/s you may record a trace every 4 cm. The antenna and embedded electronics have a total mass of 1.7 kg.

A down-forward-looking radar altimeter (Nanoradar NRA24 24 GHz) is combined with terrain-following software UgCS (Universal Ground Control Software from SPH Engineering) to allow for precise pre-determined flight paths close to the surface. An on-board PC (SPH Engineering Skyhub) is used to connect the altimeter to the flight controller and to log the recorded GPR data. GPR antennas are powered by the UAV batteries and georeferencing of the GPR traces is done using the aircraft's GNSS receiver. Real-time kinematic (RTK)

Figure 3: Picture of the high frequency system (1 GHz shielded antenna) mounted on a commercial UAV (DJI Matrice 300 RTK) and using a radar altimeter and onboard computer for terrain following and data logging (credit Sintef Industri)

positioning can also be used to enhance the precision of position data if needed. Pictures of the two GPR systems mounted on the UAV are displayed in Figure 3.

2.2 Data Pre-Processing Workflow

To enhance the readability of the data, several pre-processing steps are necessary. You can clearly see it on Figure 4 where the different steps described below have been plotted. This presentation of the workflow is largely inspired by Dupuy et al. [5] who coded it.

Step 1: Even if the aircraft flight speed is pre-programmed to be constant between waypoints, small variations in speed are still present due to wind and adjustments in flight altitude. The first step consists of extracting profiles between each waypoint and performing spatial interpolation at a regular distance based on GPS coordinates.

Step 1b (optional): The profile can be over-sampled to compensate for non-optimal time range choice when the time range is too large compared to the actual reflection times but also to give to the trace a more natural way. It then gives the impression of getting a better vertical resolution (by increasing the number of pixels)

Step 2: Time zero correction is done to adjust all traces to the same virtual time zero of the source antenna. This step crops the direct air signal by calculating the associated time based on a given amplitude threshold.

Step 3: Background removal is carried out by calculating a mean trace over the full profile and subtracting it from every trace. This step is enough to remove most of the low-frequency content and the source ringing effects.

Step 4: Band-pass filtering is done with a Butterworth filter to remove additional low and high-frequency noise, if needed.

Step 5: Amplitude correction (gain) is crucial to boost late arrival amplitudes and to correct for geometrical spreading (use of a power gain).

Step 6: Deconvolution following the approach of Schmelzbach and Huber [6]. This step is time-consuming for large profiles but is useful to derive true amplitude reflections by deconvolving the signals from the source wavelet effect. It also allows us to obtain the source wavelet of the data which will be useful for the training of the neural network to derive permittivity.

Step 7(optional): A static correction is done for topography correction by shifting each GPR trace by the relative two-way travel time of propagation in the air from the relative altitude of the UAV with respect to the take-off altitude.

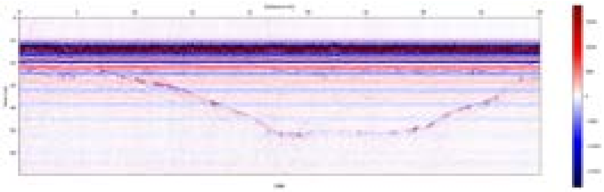

(a) Step 1: Extraction of raw data for segment 2

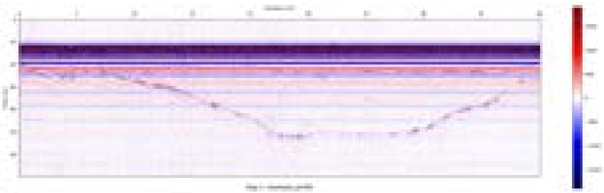

(b) Step 1b: Resampling

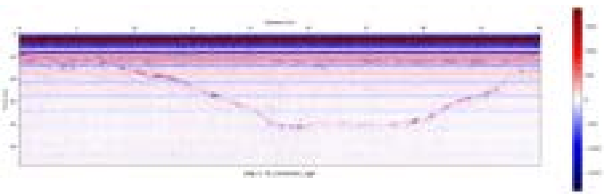

(c) Step 2: T0 correction

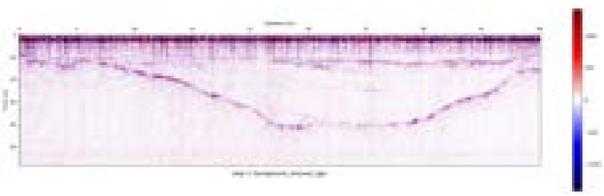

(d) Step 3: Background removal

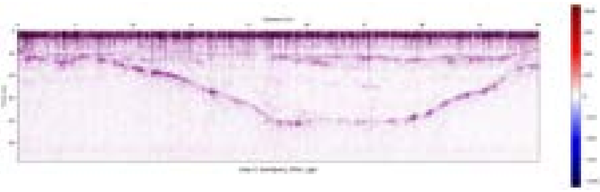

(e) Step 4: Bandpass filter

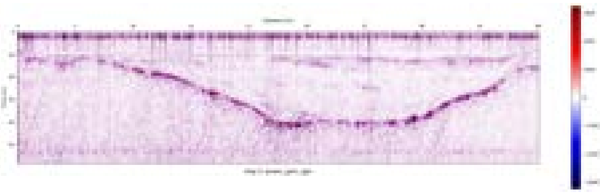

(f) Step 5: Power gain

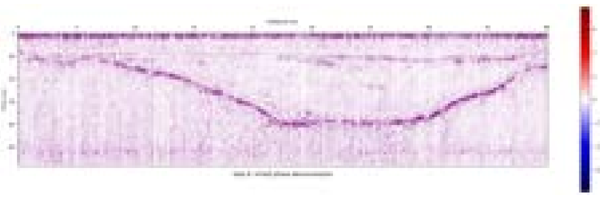

(g) Step 6: Mixed phase deconvolution

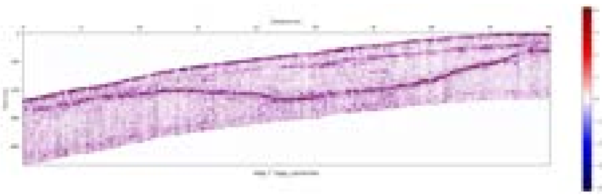

(h) Step 7: Topo correction

Figure 4: Pre-rocessing workflow, coded by Grøver and Dupuy[5], on a Storlidalen segment taken in 2022

2.3 Algorithm Development and Implementation

2.3.1 Fundamentals of GPR Wave Propagation

To explain the algorithm used to derive snow height from Ground-Penetrating Radar (GPR) data, it is essential to first comprehend the significance of the obtained GPR data. As illustrated in Figure 4g, the air-snow interface at the top and the rock/snow interface at the bottom are detectable due to significant variations in permittivity. At the interface between two media, the electromagnetic wave experiences transmission and reflection—phenomena that are well understood. To elucidate the principles of this physical phenomenon, we will examine the simple case of normal incidence of an electromagnetic (EM) wave crossing the interface between two media.

Assuming the medium is free of charge and current ($\rho = 0$ and $\mathbf{j} = 0$), we can rewrite Maxwell's equations as follows:

$$\begin{cases} \nabla \cdot \mathbf{E} = 0 \quad \text{(Maxwell-Gauss)} \\ \nabla \cdot \mathbf{H} = 0 \quad \text{(Maxwell-Flux)} \\ \nabla \times \mathbf{E} = -\mu \dfrac{\partial \mathbf{H}}{\partial t} \quad \text{(Maxwell-Faraday)} \\ \nabla \times \mathbf{H} = \epsilon \dfrac{\partial \mathbf{E}}{\partial t} \quad \text{(Maxwell-Ampere)} \end{cases} \tag{1}$$

Where $\frac{\partial}{\partial t}$ is the partial derivative with respect to the time,$\mathbf{E}$ is the electric field, $\mathbf{H}$ the magnetic field strenght ($H = B/\mu$ with $\mathbf{B}$ the magnetic flux density), μ the magnetic permittivity and ϵ the electric permittivity in the medium considered.

Epsilon is a complex number such as $\epsilon = \epsilon'' + \epsilon'$, but we neglect the imaginary part (which means no attenuation) such as: $\epsilon = \epsilon'$. Additionally, we neglect the influence of conductivity ($\sigma = 0$). These assumptions are quite accurate for dry snow (the medium under study) and for certain types of rocks (Lavoué [14], p.40). However, for wet snow, even if ($\sigma \approx 0$ in pure water), we must account for the absorption due to the imaginary part of water permittivity (see Figure 5). This attenuation, combined with the high permittivity of water ($\epsilon' = 80$ at 1 GHz), significantly reduces the penetration depth of the GPR signal.

In order to understand what happen when the GPR wave strike an interface, lets consider a wave striking an interface between two different media with normal incidence. The direction (Oz) is perpendicular to the interface. Given the rotational symmetry about the (Oz) axis, the distinction between transverse magnetic (TM) or transverse electric (TE) polarization is unnecessary because both are analogous. To simplify, let's focus on the TM case (Figure 6).

The continuity of total fields implies:

$$\begin{cases} E_1^+ + E_1^- = E_2^+ + (E_2^-) \\ H_1^+ + H_1^- = H_2^+ + (H_2^-) \end{cases} \tag{2}$$

Here, the terms in parentheses correspond to an incident wave originating from the right, coming from medium 2. This wave is not considered, as we are only interested in how a wave

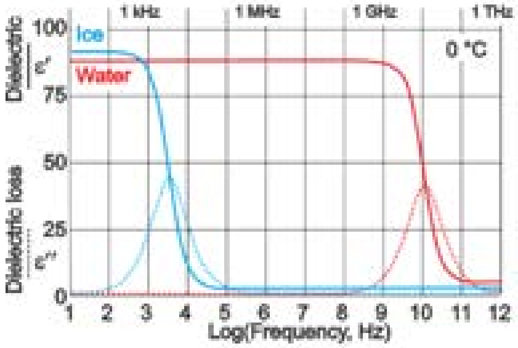

Figure 5: Permittivity of ice and water (Chaplin [15]) with respect to frequency. Note that for the 1 GHz antenna, $\epsilon'' = 0$ for ice and $\epsilon'' > 0$ for water.

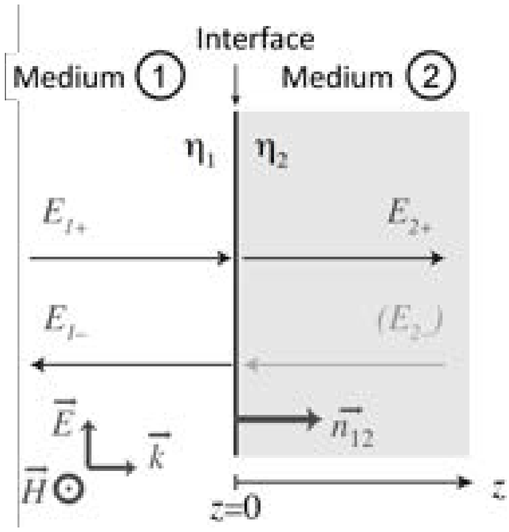

Figure 6: Electromagnetic wave striking a diopter with normal incidence (from Grandin lecture)

originating from medium 1 (E_1^+) is transmitted into medium 2 (E_2^+) or reflected back toward medium 1 (E_1^-). By using wave superposition and Maxwell-Ampere equation the total fields can be expressed (disregarding the temporal component of the fields, which is the same for all waves) as :

$$\begin{cases} E(z) = E^+(z) + E^-(z) \\ H(z) = \dfrac{1}{\eta}\left[E^+(z) - E^-(z)\right] \quad \text{where} \quad \eta = \sqrt{\dfrac{\mu}{\epsilon}} \end{cases} \tag{3}$$

By using this equation in (2), we obtain:

$$\begin{cases} E_1^+ + E_1^- = E_2^+ \\ \dfrac{1}{\eta_1}\left[E_1^+ - E_1^-\right] = \dfrac{1}{\eta_2}E_2^+ \end{cases} \tag{4}$$

Introducing the reflection coefficient (ρ) and the transmission coefficient (τ), we obtain the following equations:

$$\rho = \frac{E_1^-}{E_1^+} \quad ; \quad \tau = \frac{E_2^+}{E_1^+} \tag{5}$$

Which lead to the Fresnel formulas:

$$1 + \rho = \tau \quad ; \quad \rho \ = \frac{\eta_2 - \eta_1}{\eta_2 + \eta_1} \quad ; \quad \tau = \frac{2\eta_2}{\eta_2 + \eta_1} \tag{6}$$

Which can be reformulated by neglecting magnetic permeability (μ) variation:

$$\rho = \frac{\sqrt{\epsilon_1} - \sqrt{\epsilon_2}}{\sqrt{\epsilon_2} + \sqrt{\epsilon_1}} \quad ; \quad \tau \ = \frac{2\sqrt{\epsilon_1}}{\sqrt{\epsilon_2} + \sqrt{\epsilon_1}} \tag{7}$$

Thus, for small permittivity variation ($\epsilon_1 \approx \epsilon_2$), the entire wave is almost transmitted ($\rho \approx 0$ and $\tau \approx 1$). However, for large variations, such as between air ($\epsilon_r = 1$) and ice ($\epsilon_r = 3$) or between ice and rock (for granite $\epsilon_r \approx 4 - 6$ [14], p.40) , a fair part of the EM energy is reflected at the interface. Thanks to this brief and idealized introduction to reflection, we can better understand why significant reflections occur at the air-snow interface and the snow-rock interface. To build a more accurate model, we should consider a multilayer model, account for the angle of incidence and its impact on reflection and transmission, diffraction due to scattering points, and even interferences. However, we will not delve further into these calculations, as they are not the focus of this paper. Instead, we will refer to the model made by Garambois (from the University of Grenoble), which we will use in the second part of this study when creating models (pair of velocity profile and synthetic wave trace) to train a neural network. To justify this approach, we should also recall that permittivity variations are directly correlated with EM velocity variation since $c = c_0/\sqrt{\epsilon_r}$ where c_0 is EM velocity in the air.

2.3.2 Description of the Automatic Picking Algorithm

The obvious consequence of high reflection and signal intensity at the main horizons is the need to employ an algorithm that pick where the signal amplitude exceeds a given threshold. Therefore, we naturally opt for such an algorithm. However, a significant challenge in this automatic picking process arises from potential outliers, as some traces of the profile are subject to noise (e.g. scattering points, non GPR EM signal like telephone network etc..). Consequently, we refined our algorithm to ensure an accurate selection of the horizons (see the different steps explained below on Figure 7).

Step 1: We use the drone's altimeter, which provides an approximate distance between the drone and the snow surface, to select a time window around this estimated horizon for threshold-picking.

Step 2: a) Normalize the traces within the window using MinMaxScaler. b) Pick the first point that reaches the threshold called t_{AS} for "threshold air-snow" (read "Appendix 1: thresholding notebook" for more details). c) Suppress outliers by considering the deviation of the

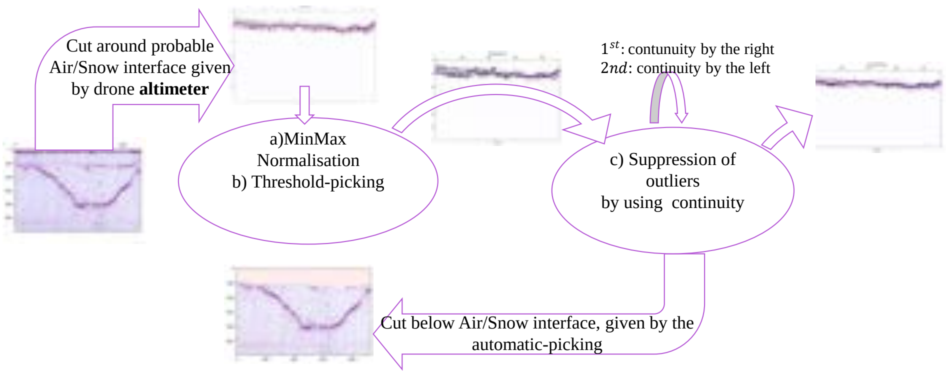

(a) Step 1-2-3: Air-Snow interface picking

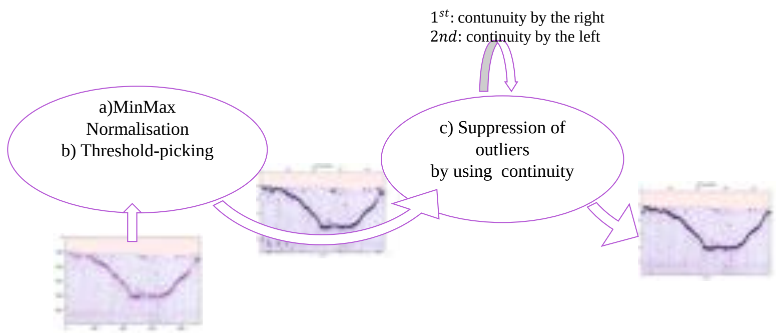

(b) Step 4: Snow-Ground interface picking

Figure 7: Scheme of principle of automatic picking algorithm (a) Air-Snow interface picking (b) Snow-Rock interface picking

punctual picks from a moving average, with increased smoothing where picking is discontinuous.

This last step (2.c) is performed twice: first using a left-deviated window to calculate the moving average for ensuring continuity to the right, then using a right-deviated window.

Step 3: Using the picking of the air-snow interface, cut the profile to keep only the part below this horizon. This step will prevent from picking twice the same interface and is therefore interesting for the picking of the snow-rock interface.

Step 4: Repeat Step 2 for the Snow-Ground interface with adjusted parameters, such as a higher threshold and reduced smoothing of the moving average (i.e.,use of a smaller window for the computation of the moving average).

- 3 -
TESTING AND RESULTS

3.1 Field Site Description

During the winter and spring seasons of 2022 and 2023, a large number of tests has been carried out at different sites in Norway. Here, we will test our automatic-picking algorithm on three of these sites located in central and western Norway (Figure 8 (top left)) which covers different types of snow conditions. The goal is to analyze the reliability of an automatic picking with a wide range of variation. This field site description was written using the pictures and information from Dupuy et al. [5].

Figure 8 provides pictures of the sites.

Storlidalen : Storlidalen is located in Oppdal municipality, in Trøndelag county (see Figure 8 (top left)). The test site is located at the western end of the valley at 620-630 meters above sea level (masl). The field site is characterized by an ESE facing slope where eastward dominant winds play a major role in snow distribution, leading to large variability in snow depths between the top of the slope (western part, close to bare ground due to snow drift eastward), the middle of the slope (maximum snow depth due to snow transport from west) and the bottom of the slope (eastern part, almost no snow accumulation; see Figure 9a).

Fonnbu : Fonnbu is located in the Stryn municipality in Vestland county (see Figure 8 (top left)). The site is located in the alpine valley of Grasdalen at 930-940 masl near the avalanche research station of the Norwegian Geotechnical Institute (NGI). The station is mostly sheltered from the dominant eastward winds by Sætreskarsfjellet summit on the west (1606 masl). The ground is mostly granit with visible rocks and water (which turn into ice in winter). UAV-borne GPR surveys have been carried out in March 2022, March 2023 and March 2024 but we will only use data from the two last surveys.

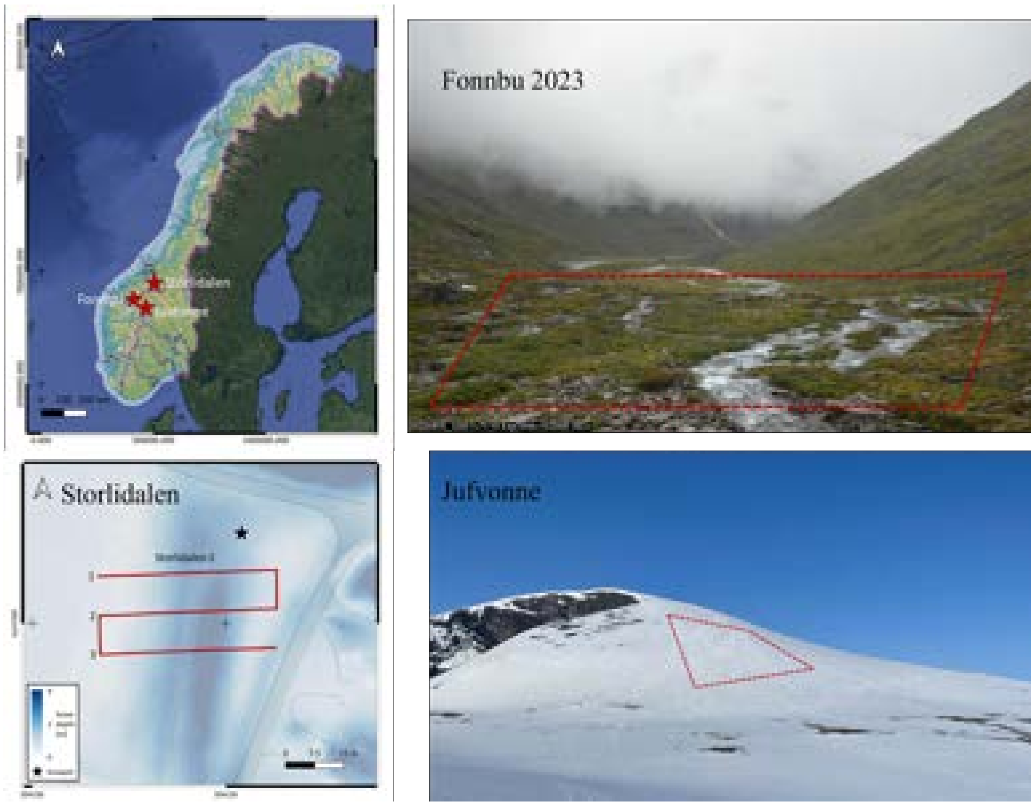

Figure 8: Top left: overview map of the field site locations. Top right: Picture of Fonnbu in summer to visualize the presence of rock on the field. Bottom left: map of Storlidalen including location of GPR surveys (red lines) and snowpits (black stars).The background map combine contour lines and snow depth derived by UAV-borne LiDAR surveys. Bottom right: picture of the field site in Jufvonne.

Juvfonne : Juvfonne field site is located in Lom municipality, which belongs to Innlandet county (see Figure 8 (top left)). The site comprises a glacier patch located between 1852 and 1958 masl (2019 mapping) and which has been monitored with mass balance measurements since 2010 [62]. The terrain is steep (between 20 and 35 degrees) and is representative of alpine terrain with lateral relief variations.

3.2 Validation Methods

3.2.1 Validation Method for Automatic-Picking

To validate our automatic method, two methods were envisaged:

- The comparison with a manual picking on different field data ;
- The comparison on a large scale results with LiDAR data.

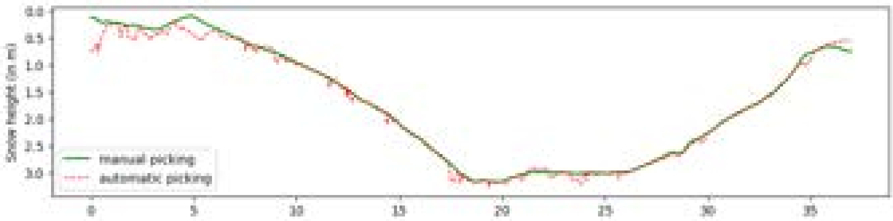

(a) Storlidalen, 2022, homogeneous grassy field in slope(see Figure 8), antenna 1GHz

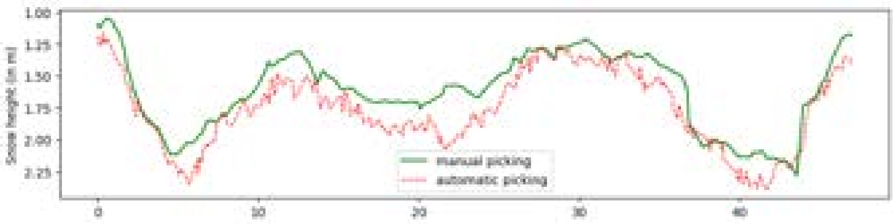

(b) Fonnbu, 2023, heterogeneous rocky field in valley(see Figure 8), antenna 1GHz

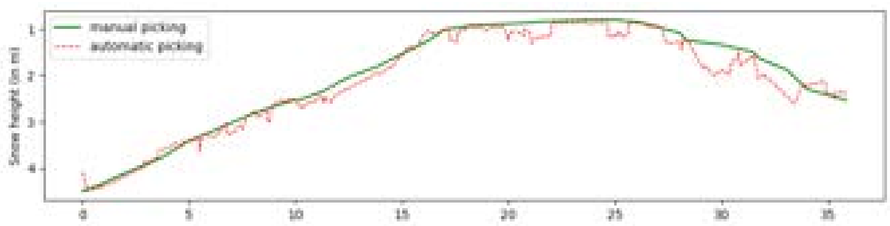

(c) Jufvonne, 2023, homogeneous rocky field in slope(see Figure 8), antenna 400MHz

Error comparison table with Manual picking as a reference			
	Mean Absolute Error (in cm of Snow)	MAE (in %)	Mean Relative Error(in %)
Jufvonne	14cm	7%	+3%
Fonnbu23	15cm	9%	+9%
Storlidalen	6cm	3%	+2%

(d) Table comparing the absolute and relative error in cm of snow and in % of of the average snow height (see detailed errors in Annex)

Figure 9: Comparison between manual picking and automatic picking in terms of(top) snow height and (bottom) absolute snow difference (by using an averaged relative permittivity in the snow of $\epsilon = 2$

The primary objective of developing this automatic-picking algorithm was to automate a process that was initially performed manually. Once its consistency with manual picking is established, we will apply it to a larger dataset, which is currently impractical to analyze manually due to time constraints. This section will compare the algorithm's results with manual picking, while a subsequent section will discuss the comparison with LiDAR data on a larger scale.

To facilitate the comparison between manual and automatic picking, we estimate snow height. We approximate the EM velocity in snow as constant ($c = c_0/\sqrt{\epsilon_r}$ with $\epsilon_r = 2$), providing an initial error estimate in snow height. Although this is a strong approximation, it gives us a reasonable error estimate in snow height, our ultimate parameter of interest. Additionally, we compute the percentage error, which is independent of this approximation and consistently yields a Mean Absolute Error of less than 10% (see Figure 9). We will show later how we can derive permittivity from the GPR profile and obtain a more accurate snow depth prediction (3.3.2 GPRNet Results).

It is important to note that achieving these results required adjusting the input parameters for different field cases, particularly the approximate minimum snow height ($Snowheight_{min}$). This adjustment aids the algorithm in identifying the second main horizon, which should correspond to the snow-rock interface. For instance, in Jufvonne(Figure 9c), setting a larger minimum snow height prevents confusion between snow intern reflections and snow-rock reflections, whereas in Storlidalen (Figure 9a), a lower minimum snow height is necessary to correctly identify the bedrock on the left side (almost 0cm).

Therefore, while the algorithm is not entirely automatic and requires appropriate input parameters to function effectively, these inputs do not require substantial changes. Instead, minor adjustments to the $Snowheight_{min}$ and thresholds for the air-snow interface (t_{AS}) and snow-rock interface (t_{SR}) are sufficient to achieve reliable results(further details of the imput parameters in the "Appendix 1: thresholding notebook")

To account for the uncertainty in manual picking, we conducted two manual pickings on the same segment to identify challenging areas. Figure 10 highlights these difficult-to-pick regions. In some locations, it was challenging to determine the exact rock-snow interface. Therefore, we performed two types of picking: one aimed at identifying the highest plausible rock-snow horizon and another at the lowest plausible horizon (while maintaining relevance). Although this approach is not rigorous to account for picking uncertainty, it serves as a reminder that manual picking is not always an absolute reference, especially in rocky terrains.

To conclude, we can briefly summarize the hypotheses made to build this algorithm:

1. For each trace, there is always one point (and only one) where air meets snow and one point where snow meets rock.

2. There are strong reflections at the air-snow and snow-rock interfaces.

3. The interfaces are continuous.

4. The snow is dry.

We can then provide examples where our algorithm will need refinement. If there are locations in the profile where there is no snow, hypothesis 1 is no longer valid. Additionally,

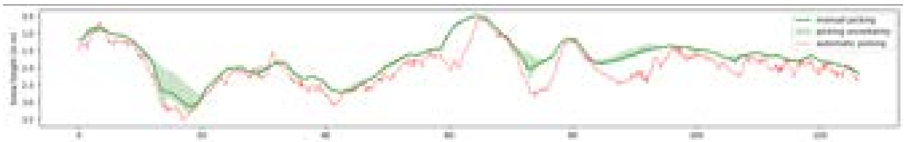

(a) Fonnbu, 2024, rocky field, antenna 1GHz

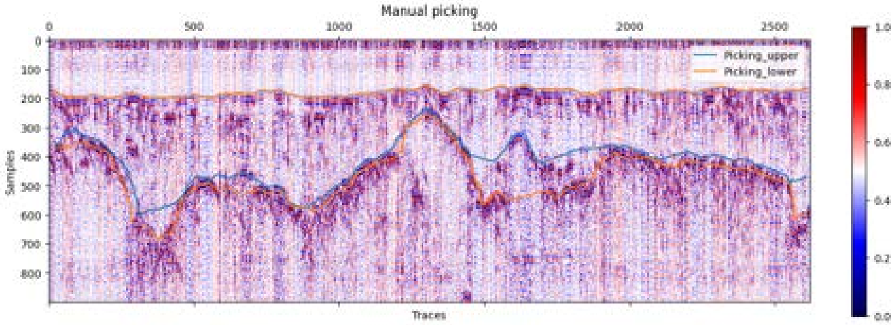

(b) Fonnbu, 2024, GPR profile

Figure 10: Comparison between manual picking and automatic picking in terms of snow height by using an averaged relative permittivity in the snow of $\epsilon_r = 2$

it is less effective on very light snow due to its reliance on reflection intensity (hypothesis 2). Indeed, when the initial snow layer is so light that it has a permittivity almost identical to air, a stronger reflection may occur at the light snow-dense snow interface rather than the air-snow interface. There is finally one last issue that should be addressed: the algorithm tends to pick slightly below the manual picking results (see Figure 9b and in the Figure 9d), which may lead to an overestimation of the snow height. We will see what error it can leads to in the computation of the snow height in part 3.3.1.

3.2.2 Validation Method for CNN Velocity Prediction

1. **Min-phase wavelet extraction:** In Section 2.2 (Data Pre-Processing Workflow), we discuss the deconvolution step, which is also pertinent for extracting the source wavelet of the signal. It is crucial to use a source wavelet that closely approximates the real one. To maintain generality, we performed the source wavelet extraction on 1000 traces from several surveys (Storlidalen2022, Fonnbu2023, and Fonnbu2024) using the same antenna (see Figure 11). We then averaged these wavelets, which were consistent with each other, apart from some ringing effects that were removed to retain generality. We finally obtained a wavelet which looks like an asymmetrical 'Ricker' wavelet(see Figure 11) with a mean frequency of 0.8 GHz (<1GHz due to some loss of energy). We tested the wavelet on different profiles of snowpack using an mdem hardcoded algorithm developed by Garambois et al., inspired by Irving and Knight [13]. Mdem is a modelling tool which is computing EM wave propagation in a stratified medium with a propagator matrix method. It allows fast calculation of the GPR signal compared to conventionnal finite

difference approaches and is valid for zero offset data such as drone GPR data where we locally neglect horizontal heterogeneities.

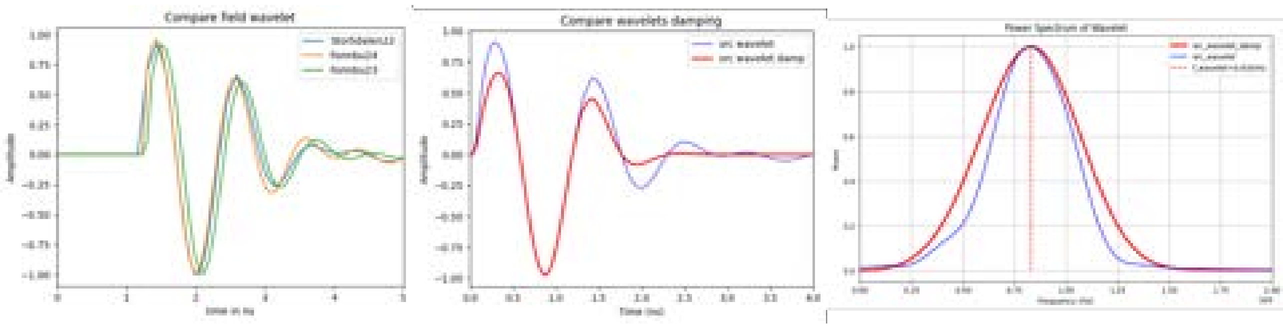

Figure 11: (left) Comparison of the min-phase wavelet extracted from different surveys, (middle) comparison of the wavelet before and after damping in the time domain, and (right) in the frequency spectrum obtained after Fourier transform.

Parameters used for random snowpack generation											
			Number of snow layers		Snow					Basement	
Time window	Nsamples	z_max	n_max_layers	n_min_layers	thick_min	thick_max	dz_min	ep_min	ep_max	ep_min	ep_max
70 ns	1024	6m	13	3	0.5m	5.5m	0.025 m	1.3	2.2	4	8
Type of random distribution			uniform		normal*			normal*		uniform	
					Velocity associated in (m/ns):			0.263	0.202	0.150	0.106

Table 1: Overview of the parameters used in the snowpack random generation and their associated random distribution (* for normal distribution 95% of the values should be contained between the min and the max)

2. **Random production of 50,000 models of pairs of snowpack profile and their associated synthetic GPR trace:** Once satisfied with our wavelet, we used it to generate pairs of models (snowpack profile plus associated traces generated by mdem). To achieve this, we first defined the parameters of the function to create a random snowpack profile (function implemented by Arnt Grøver where I just had to modify parameters and distribution function to optimize the training) with a random number of snow layers and random permittivity (see Table 1 for more details). We aimed to keep the model as physical as possible without overfitting by using data too similar to what we intended to find. One might question why synthetic data is used. The primary issue is the lack of sufficient real data for training a neural network, making synthetic data necessary. After generating the synthetic dataset (10,000 models takes 5 hours), we augmented it by adding 4 different random sinusoidal noises (within the bandpass filter range used for the real data) to each trace, resulting in 50,000 different models but only 10,000 different velocity profiles. The idea was to show to the CNN that the same velocity profilein the snowpack could lead to different signal trace due to the noise. One can visualize a pair of velocity profile and trace associated before and after the adding of the noise on Figure 12. You can clearly see on both traces that large variation in velocity profile lead to

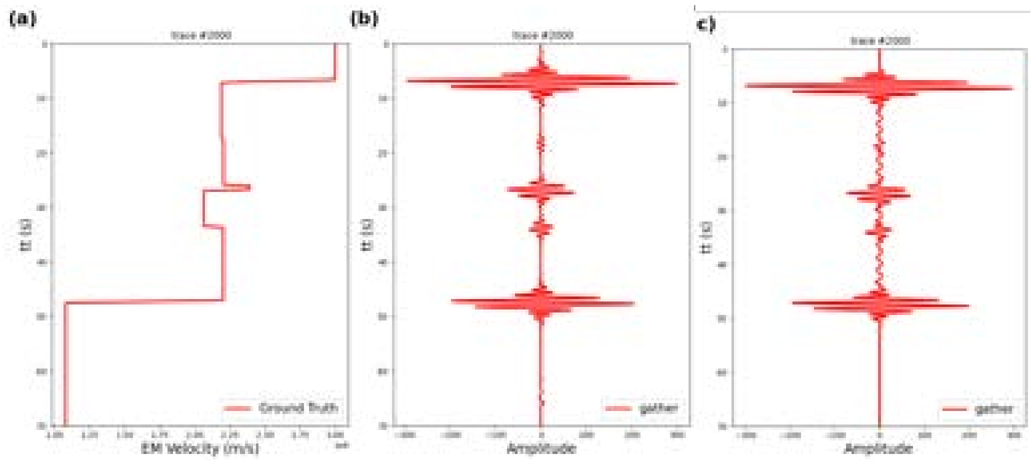

Figure 12: (left) random snowpack from the dataset, (middle) associated trace before transformation, and (right) after random noise addition.

large amplitude as it was supposed. Additionally, we applied a spatial filter to attenuate the trace before the air-snow interface and after the snow-rock interface to focus on the snowpack. This approach demonstrated to the neural network that multiple traces could exist for the same snowpack due to noise.

3. **Training and testing of the CNN on the synthetic data:** To derive permittivity variation, we employed an encoder-decoder-based convolutional neural network (CNN) called GPRnet developed by Leong and Zhu [12]. The CNN utilized the DeepLabV3 architecture, known for its accuracy in feature extraction from images. We split the synthetic data into training, validation (99% of the data), and testing (1% of the data) sets. The dataset is composed by 50 000 models generated before, in each model the signal trace is composed by 1024 points which represent the features and the velocity profile is the label. The training and validation yielded good results ($R^2 = 97\%$ after 5 hours of training, see Figure 13), and tests on synthetic data showed high accuracy too ($R^2 = 97\%$). We can well visualize on Figure 13 that the neuron network is able to reproduce with good approximation the velocity profile except some small variation.

4. **Testing on real data:** The initial step with real data is preprocessing to make it resemble the synthetic data: resampling to be on the same time range (with 1024 samples), t0 correction, and reshaping to include only 1 meter of air (the synthetic data is generated by assuming that the drone GPR is always located at 1m above the snow surface)) and attenuating before and after the snowpack. This is feasible now that the air-snow and snow-rock interfaces are known. However, power gain adjustments are unnecessary as our model accounts for geometrical spreading. The primary challenge when testing on real data is verifying the accuracy of the profiles generated. At the beginning the verification was only visual, and we could improve our training and refine the models. Nevertheless, we could also validate quantitatively the average velocity found for each trace by comparing it with LiDAR data and examining the patterns identified, especially when a light snow

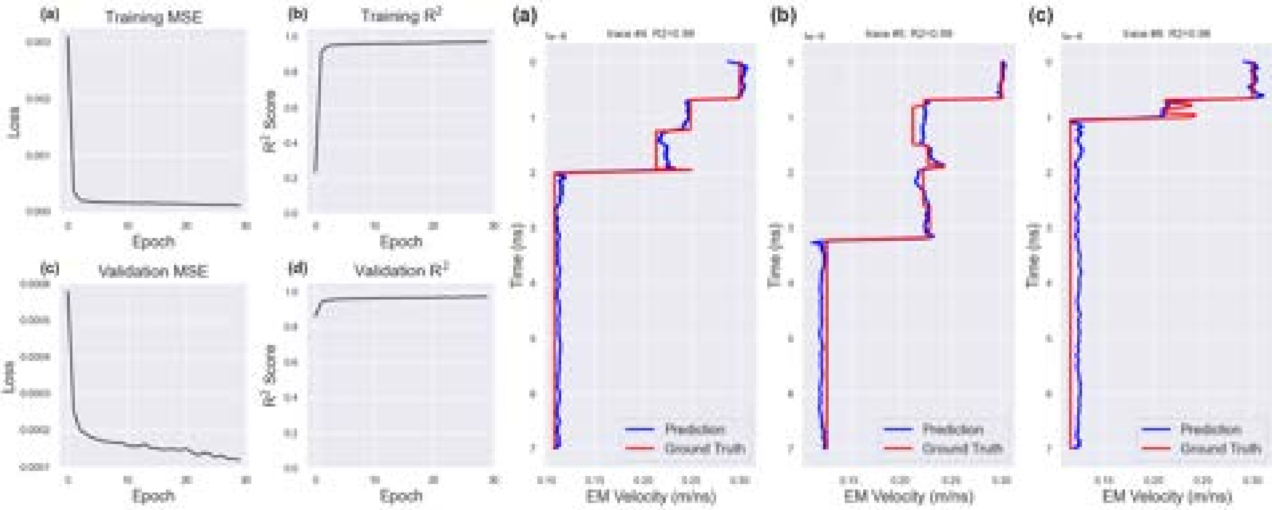

Figure 13: (left) Results, in terms of loss by calculating (mean square error (MSE)) and R2 score, obtained on training set and testing with respect to the number of epochs and (right)Random Snowpacks velocity profile from the test set and the CNN prediction associated

layer exists on a dense layer. This will be discuss further in 3.3.2 GPRNet Results.

3.3 Results

3.3.1 Snow Depth Large Scale Results

Given that our picking algorithm achieved a mean absolute error of approximately 10% during initial validation, we deemed it suitable for subsequent comparisons of snow depth predictions with LiDAR data. We must first recall that LiDAR uses a laser(wavelength between 600 and 1000 nm) which is ideal for surface modeling whereas GPR (wavelength between 0.3m and 30m) excels in subsurface imaging and detection, revealing hidden structures. This comparison necessitated breaking the process into multiple steps. Prior to executing the full procedure, we rigorously tested the first two steps on a few segments to fine-tune the parameters and estimate the required processing time. The dataset comprised 100 profiles, each containing 2.5 million pixels (900 x 2600), necessitating meticulous step-by-step optimization to ensure timely processing. This dataset represents a 40m x 130m area (see Figure 14), emphasizing the need for computational efficiency.

1. **Pre-processing of the dataset (as described in Section 2.2):** To optimize calculations, we utilized only the initial five steps (see Figure 4), as the mixed-phase deconvolution significantly increased processing time by several minutes per segment and was not essential for the picking process. Ultimately, processing the entire dataset (250 MB) took approximately 15 minutes using a computer with a Ryzen 5 processor and 8GB of RAM.

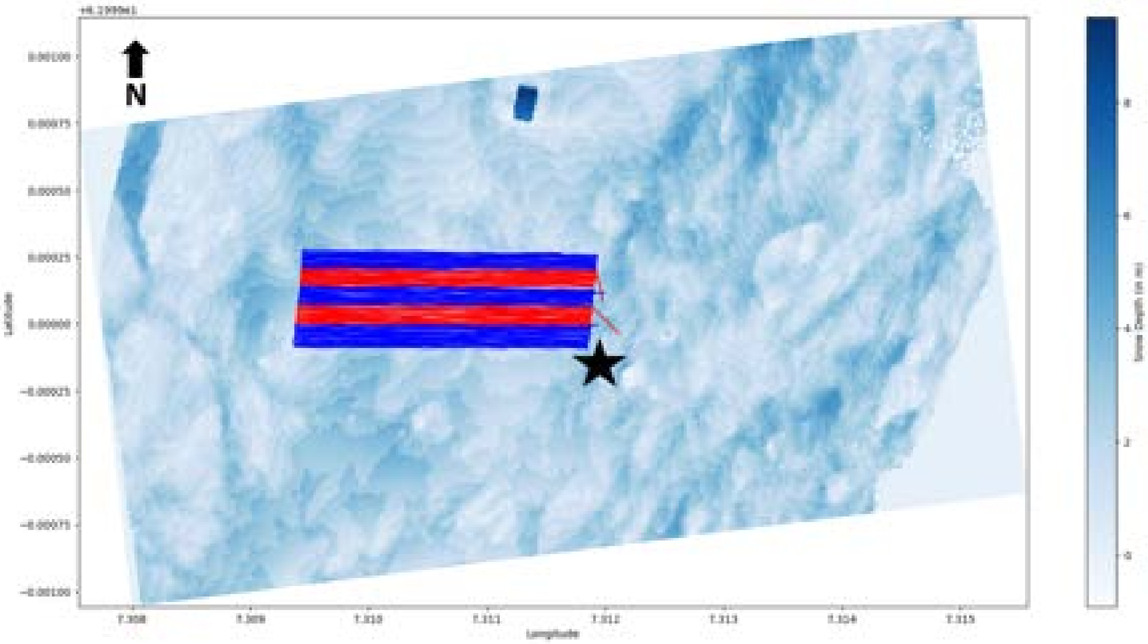

Figure 14: Fonnbu 2024 field survey(blue and red lines represent the GPR lines flown in 5 different surveys). The total GPR survey area is 40 by 130 m, and GPr lines are spaces every 0.5 m. The background map is the snow depth derived by UAV-borne LiDAR survey. The black star is the location of the snowpit we use to derive a velocity profile (see Figure 12) and the blue rectangle the NGI avalanche research station

2. **Picking of the main interfaces:** Minimal parameter adjustments were required for our algorithm to align with the 2024 Fonnbu survey. The choice of a simple thresholding algorithm combined with dimensionality reduction proved effective, completing the entire survey in just one minute. This picking gives us the two way travel time of the wave in the snow and to convert into a snow height we need the EM velocity.

3. **Estimation of the average velocity in the snow:** This step was first achieved by deriving permittivity profile from a snowpit density profile made on the zone. Our goal was to determine an objective average velocity for use throughout the entire survey. This approach is similar to the validation method described in section 3.2, but in this instance, we used a snowpit where a density profile was measured to calculate the velocity profile (see Figure 15). The figure on the left(on Figure 15) shows a synthetic snow density profile generated by the Snowpack SLF simulator using 2021 meteorological data from Stryn. The approximation made by discretizing the density profile into a small number of layers (as shown on the middle) is evident. However, the density measurement was precise, calculated by averaging two or three measurements. Given our goal of obtaining an average velocity for the snowpack, this level of precision was sufficient for our needs.

   To derive velocity from snow density, we employed the empirical formula $c = c_0/(1 + 0.85\rho)$, where ρ is the relative density, c_0 is the EM velocity in the air, and c is the EM velocity in the snow($c = c_0/\sqrt{\epsilon_r}$). This formula is considered the most general according to Di Paolo et al. [4], who conducted a critical review of existing permittivity formulas. Ultimately, we obtained an average velocity in the snow of 22 ± 2 cm / ns, which means $\epsilon_r = 1,9 \pm 0,3$.

We also use the GPRnet prediction to measure snow height (15s for one profile) but we did not expand it on the whole dataset because there was not strong variation between GPRNet prediction and snowpit one. However this is still an interesting way to go further in snow height measure and we will try to measure the velocity prediction accuracy in 3.3.2 GPRNet results (but on an easier dataset: Storlidalen). To visualize GPRNet results on Fonnbu2024 dataset you can read "Appendix 3 : GPRNet prediction notebook".

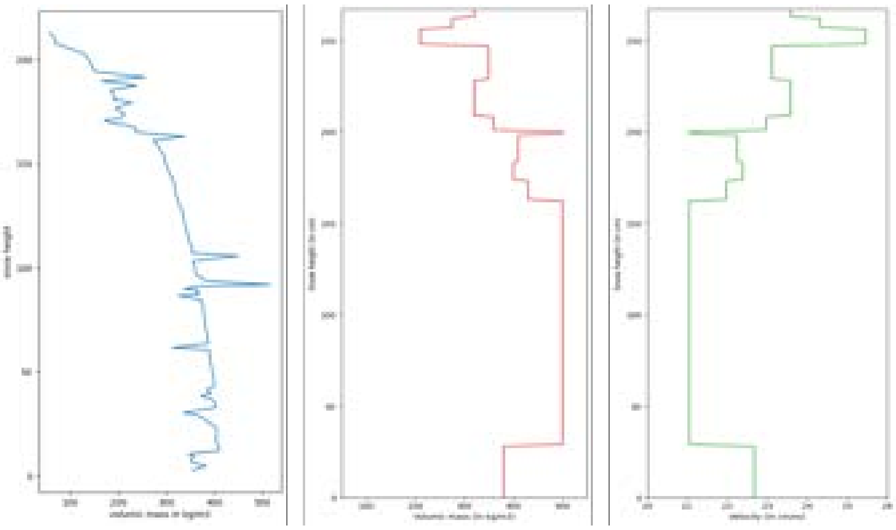

Figure 15: (left)Simulated snowpack with snowpack slf simulator (Bavay and Egger [16]) thanks to Stryn meteorological(2021) data, (middle) density profile measured during a snowpit by discretizing the snowpack in a snow pit of 2.7m depth digged in Fonnbu on march 2024 [17], in the snow we can visualize the 13 layers of the snowpack and (right) Velocity profile from which we find an averaged velocity of $c_{avg} = 22 \pm 2cm/ns$

4. **Interpolation of GPR results and interpolation of the LiDAR data on a 2D map:** This step posed the greatest challenge due to the need to identify a cost-effective interpolation predictor capable of handling snow depth data. For instance, applying kriging interpolation to a dataset of 50 segments, each containing 125 snow depth points (totaling 6000 points and 1mx1m grid resolution), took 1.5 minutes, while interpolating 2500 points required only 15 seconds. This interpolation was performed on a lozenge grid (60x300 pixels) with a resolution of 0.7 m x 0.4 m pixels. For more details, see "Appendix 2: interpolation notebook". To compare LiDAR data with GPR data interpolated we had to somehow resample LiDAR snow map to make it fit GPR data. That is why we tried to perform the same interpolation as the one conducted on GPR.

5. **Comparison of interpolations and data:** We first compared different interpolation

methods, focusing on Ordinary Kriging and Radial Basis Function (RBF) interpolation after considering the different possible interpolation presented by Mitas and Mitasova [18].

Ordinary Kriging and RBF interpolation are established methods for predicting unknown values from spatially distributed data. Ordinary Kriging employs a variogram to model spatial correlation, assigning weights to minimize prediction variance, thus providing accurate estimates. RBF interpolation constructs an interpolation surface using distance-based radial basis functions, resulting in a less smooth interpolation but without the need for spatial correlation modeling. Both methods are computationally intensive, with Kriging also demanding significant memory resources.

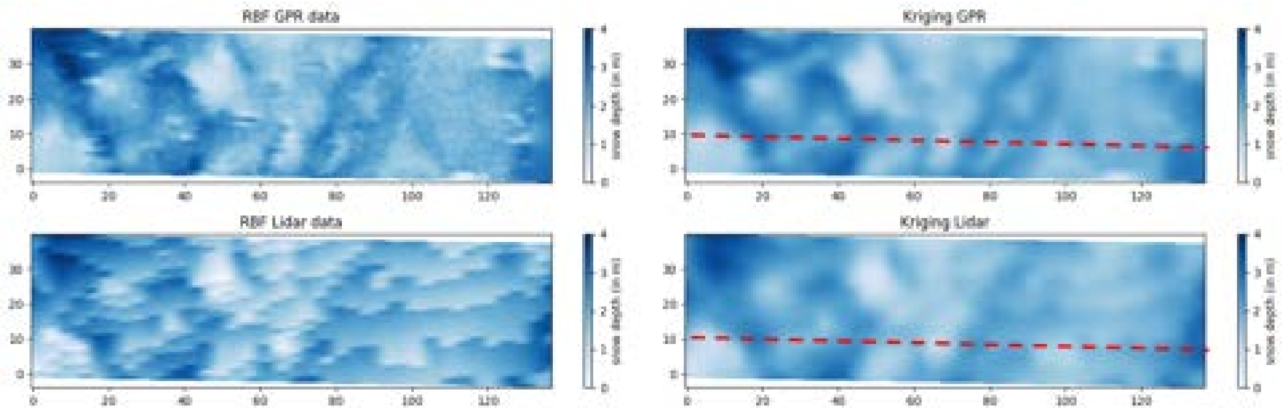

Figure 16: Comparison between GPR and LiDAR interpolation dor snow depth mapping on Fonnbu2024. On the left the map are obtained thanks to RBF interpolation and on the right thanks to kriging interpolation (absolute and relative error between LiDAR and GPR are listed in Table 2). The red dotted line represent the approximated location of the segment represented on Figure 17

We demonstrate that kriging interpolation provides the best fit to the LiDAR data by smoothing the profile and removing some artifacts, while the RBF interpolation is still useful, as it preserves raw data patterns. Figure 16(bottom left) illustrates that the LiDAR snow depth resolution is relatively low, approximately 1 meter, due to the ground truth data used. Kriging interpolation increases resolution and improves the fit between GPR and LiDAR data. We are now awaiting a new LiDAR survey in the summer to achieve better ground resolution for a more accurate comparison. However, as shown in Table 1, we achieved a snow resolution of about 20 cm (11%), which is quite good given the low resolution of the reference data.

Additionally, we compared the interpolation on a segment to evaluate whether interpolation could reduce artifacts and better align with the LiDAR reference. Although this result requires refinement once we obtain the ground truth, Figure 17 and Table 2 show that interpolation brings us closer to reality. In Figure 17, one can see the snow depth derived from manual picking, automated picking, automated picking interpolated with kriging (all three depth profiles calculated with $c = 22\,\mathrm{cm/ns}$), and LiDAR data interpolated with kriging. Notably, the interpolated GPR segment is closer to the LiDAR data (see Table 2) than the non-interpolated one, likely because the interpolated one accounts for the entire survey. Nonetheless, we still observe a significant relative error (around +6% on the entire map), indicating an overestimation of snow depth. This overestimation may be due to the automatic picking process (as we already saw in Figures 9 and 10), the velocity approximation, or the low resolution of the reference data. Furthermore, if the manual has for sure a lower relative error on this segment (-4%) its has a large absolute error(16%) so the overestimation of the automatic picking may not be sufficient to explain the observed difference. Consequently, it is difficult to draw definitive conclusions until we have more precise reference LiDAR data.

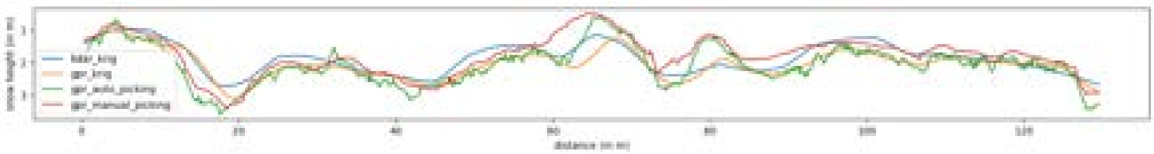

Figure 17: Comparison of snow height for manual picking, automatic picking, interpolated automatic picking and interpolated LiDAR on a segment (the same one that was considered on Figure 10 and represented by the dotted line on Figure 16). The absolute and relative error between LiDAR and GPR are listed in Table 2.

	Mean Absolute Error (in cm of Snow)	MAE (in %)	Mean Relative Error (in %)
Error comparison with Lidar as a reference on a segment			
gpr_auto_picking_rbf	25 cm	13%	10%
gpr_auto_picking_kriging	21 cm	11%	9%
gpr_auto_picking	33 cm	18%	10%
gpr_manual_picking	30 cm	16%	-4%
Error comparison with Lidar as a reference on the entire map			
gpr_auto_picking_rbf	26 cm	13%	6%
gpr_auto_picking_kriging	21 cm	11%	6%

Table 2: Overview of the relative and absolute errors in cm of snow and in % of mean snow depth with MAE= $avg(abs(SnowDepth - SnowDepth_{ref}))$

3.3.2 GPRNet Results

Having demonstrated that our CNN performs well on synthetic data, we will now present its performance on real data. We will discuss its ability to predict both the average EM velocity in the snowpack and the density variations. For average velocity prediction, we used the Storlidalen data because the ground was homogeneous, grassy and easy to pick (see Figure 9a), and we had a LiDAR snow map to serve as a reference. Figure 18 shows our ability to

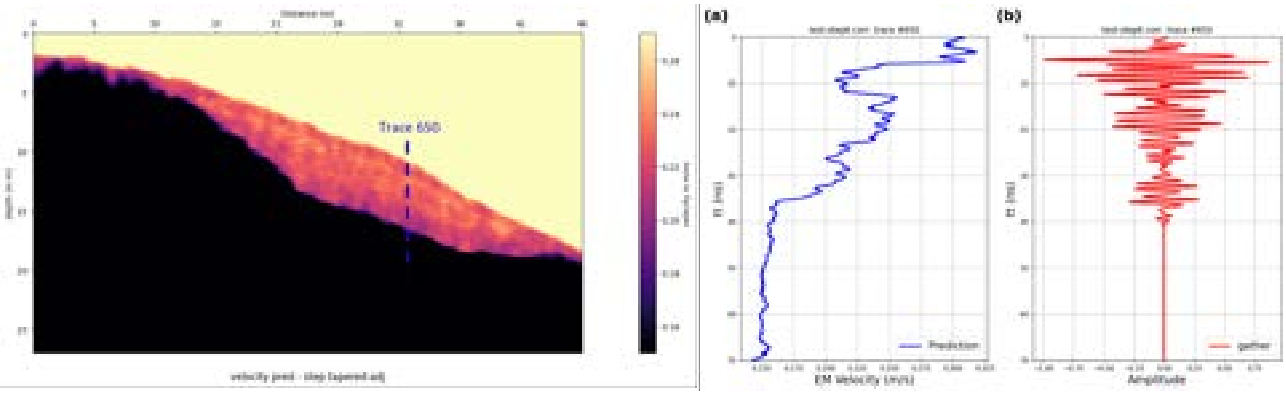

Figure 18: (left)Smooth velocity profile predicted by GPRNet in depth domain and (right) the pair of snowpack predicted from the trace assiociated

plot a velocity profile in depth domain. This was achieved by combining all the 1D velocity predictions from the algorithm (like the one plotted at the right of Figure 18), smoothing the results with a Gaussian filter, and then reshaping the profile to represent it in the depth domain. The gaussian filter is quite important because it gives horizontal continuity in the snowpack to correct the fact that the GPRNet predicts 1D models that do not take into account any horizontal continuity.

We then used this velocity profile, along with the automatic picking, to obtain the snow depth from GPRNet. We compared it with the LiDAR data (see Figure 19) and found that they are very close, even though it appears to underestimate the snow height by around 5% on average. To further analyze, we plot the velocity distribution by column of snow (900 columns, see Figure 19), noting that the maximum occurrence velocities are even closer than the mean velocities (less than 3%), which is very encouraging. To calculate this velocity distribution we used one the one hand the GPRNet prediction and on the other hand the snow depth measured by LiDAR divided by the travel time of the GPR in the snow-pack measured by the automatic picking.

To explain the difference between the histogram shapes (one has a tail to the left and the other a tail to the right), we point out that on the left side of the Storlidalen profile, we significantly underestimate the snow depth due to the large bedrock slope angle (about 40°, see Figure 18(left)). This phenomenon occurs because the beam is not perfect and corresponds to a cone, causing the shortest two-way travel time of the EM signal to be oblique rather than vertical, which can lead to significant error when the slope is steep (see Figure 23 in the appendix to visualize this error). And since this error impacts the two way travel time estimated by the automatic picking and used to calculate LiDAR velocity profile. A well-known algorithm called migration, available in RGPR ([6]), can correct this. However, this algorithm requires the EM velocity in the snow to be tested. Therefore, we have not applied it yet but will consider it to improve our results.

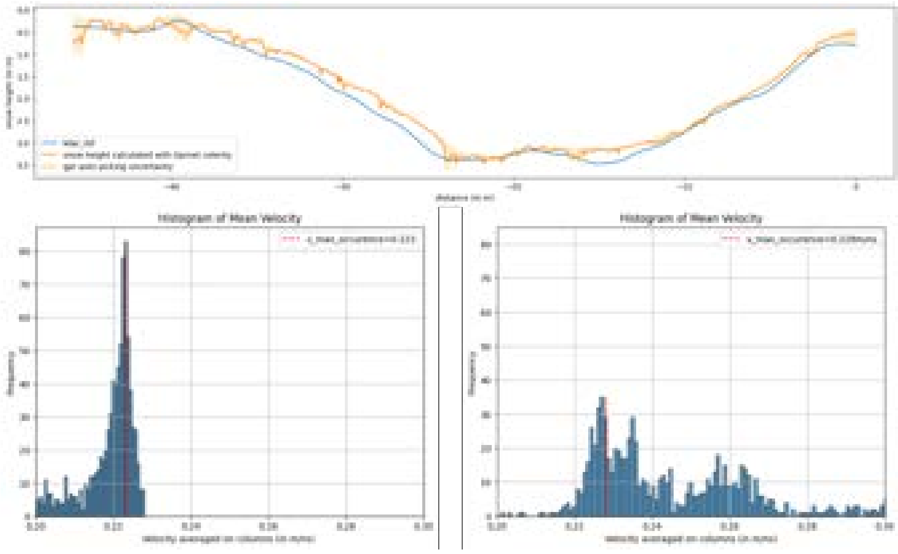

Figure 19: (top) Comparison between LiDAR snow depth interpolated with RBF and GPRNet prediction from automatic picking on the Storlidalen segment we used in Figure 18, (bottom) Histogram comparison of average EM velocity in column of snow (900 columns concerned) between LiDAR(calculated by dividing LiDAR depth measure by automatic-picking travel-time measure) and GPRNet prediction.

Finally, to verify that GPRNet can identify major velocity variations (indicating significant density differences), we tested it on a survey conducted in Fonnbu on 15 March 2023, when new snow had just fallen on the upper part of the snowpack, which was frozen and dense. This resulted in a light snow layer over a dense snow layer. In this scenario, it was easier to detect the internal interface rather than the air-snow interface (see Figure 20) because the first reflection was very light. It is noteworthy that our algorithm could identify both the light and dense layers. Indeed, you can see on the 1D profile we extracted (Figure 20 (left) that the CNN predicts well the presence of a fine dense layer(around 2.4 m depth below the drone) below a lighter layer(2.2 m-2.4 m). However, it cannot do this consistently across the entire survey(see on the profiles between 12 and 23 m), likely due to an underestimation of the bedrock permittivity(see Table 1). Because a high permittivity of the ground (which can be due to the presence of liquid water $\epsilon_r = 80$ leads to a very high reflexion which leads to a poor resolution of the rest of the trace after the normalisation by the maximum. This could be improved by increasing the number of models that account for higher bedrock permittivity.

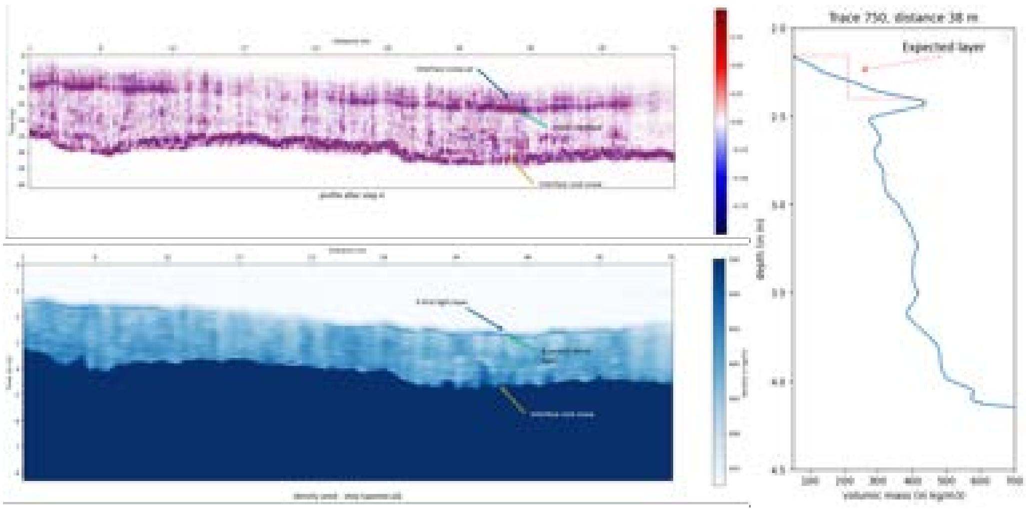

Figure 20: (Top)Data after processing(time domain),filtered before snow surface and after snow-ground interface, (bottom) Density profile depth converted and smoothed from Fonnbu2023 dataset and (right) an extracted trace to show the density variation between the light layer and the dense one (even if the profile is a bit too continuous)

- 4 -
CONCLUSION AND FURTHER WORK

This study demonstrates the effectiveness of combining unmanned aerial vehicle (UAV)-borne geophysics and remote sensing for comprehensive snowpack monitoring. The use of Ground Penetrating Radar (GPR) in conjunction with advanced algorithms has proven to be a powerful method for measuring snow properties, such as snow height and density, across large scales. By employing a Convolutional Neural Network (CNN) and automatic picking algorithm to predict electromagnetic (EM) velocity profiles from signal traces, we addressed significant challenges in automating snowpack identification and velocity profile derivation.

Our results indicate that the developed picking algorithm accurately identifies the snow surface and snow-rock interface with an error margin of less than 10%. Accuracy is notably higher on grassy or icy slopes compared to heterogeneous rocky terrains. High-density snow height estimates for a 40 x 130 m area showed good agreement with low-resolution LiDAR data, despite a 11% average absolute error likely due to limitations in automatic picking or reference data resolution. The machine learning algorithm provided effective velocity profiles consistent with LiDAR observations (with a 5% absolute error) and demonstrated reliable performance for detecting fine layers.

Despite the promising results, several challenges remain that must be addressed to improve the accuracy of our methods. First, the picking algorithm could be enhanced by incorporating variable uncertainty. This could be achieved by calculating the difference between its initial guess and the final smoothed result obtained through continuity enforcement. Such an approach would provide better confidence in snow depth mapping by indicating whether errors are due to the automatic picking process, the EM velocity predictor, or the propagation of the EM wave itself.

Furthermore, our neural network was trained with a limited range of basement permittivity values. This limitation may reduce its ability to accurately detect bedrock with liquid water, which has a relative permittivity of 80. Testing the network under such conditions and training it with a more diverse dataset could potentially enhance its robustness and efficiency.

Additionally, the velocity prediction capability now allows us to incorporate a migration step into our processing workflow. This step is crucial for converting apparent dips into true dips and for suppressing diffraction hyperbolas, thereby improving the overall accuracy of our snow depth measurements. Future work will focus on these enhancements to further refine our approach and extend its applicability to a wider range of environmental conditions.

REFERENCES

[1] F. Di Paolo, B. Cosciotti, S. E. Lauro, E. Mattei, M. Callegari, L. Carturan, R. Seppi, F. Zucca, and E. Pettinelli. Combined GPR and TDR measurements for snow thickness and density estimation. In *2015 8th International Workshop on Advanced Ground Penetrating Radar (IWAGPR)*, pages 1–4, . doi: 10.1109/IWAGPR.2015.7292642. URL https://ieeexplore.ieee.org/abstract/document/7292642?casa_token=LksMB5j4OhwAAAAA:JMYsBGZkFTH-aRDYh5dswfo4LF56o8HMS1sGbedRN5zUJEz3iLzJPVHO4V5yJK7BvIybCh3W.

[2] Alberto Godio, Barbara Frigo, Bernardino Chiaia, Paola Maggioni, Michele Freppaz, Elisabetta Ceaglio, and Paola Dellavedova. Integration of upward GPR and water content reflectometry to monitor snow properties. 16(2):154–163. ISSN 1569-4445, 1873-0604. doi: 10.3997/1873-0604.2017060. URL https://www.earthdoc.org/content/journals/10.3997/1873-0604.2017060. Publisher: European Association of Geoscientists & Engineers.

[3] Nena Griessinger, Franziska Mohr, and Tobias Jonas. Measuring snow ablation rates in alpine terrain with a mobile multioffset ground-penetrating radar system. 32(21):3272–3282. ISSN 1099-1085. doi: 10.1002/hyp.13259. URL https://onlinelibrary.wiley.com/doi/abs/10.1002/hyp.13259. _eprint: https://onlinelibrary.wiley.com/doi/pdf/10.1002/hyp.13259.

[4] Federico Di Paolo, Barbara Cosciotti, Sebastian E. Lauro, Elisabetta Mattei, and Elena Pettinelli. Dry snow permittivity evaluation from density: A critical review. In *2018 17th International Conference on Ground Penetrating Radar (GPR)*, pages 1–5, . doi: 10.1109/ICGPR.2018.8441610. URL https://ieeexplore.ieee.org/abstract/document/8441610?casa_token=5eahpyQrWHAAAAAA:inflazcdBpsOl_wuQ6pclRirSQz42Qo5yGRjA3Kq5Q3kCOccm3DAWieDGbgxZqq_2JD5HtLs. ISSN: 2474-3844.

[5] Bastien Dupuy, Arnt Grøver, Stéphane Garambois, Andrew Tobiesen, Pauline Lorand, Halgeir Dahle, Sean Salazar, Regula Frauenfelder, Benjamin Emmel, Aslak Einbu, and Tore Humstad. Uav-borne gpr for snow mapping and characterization. URL https://papers.ssrn.com/abstract=4682188.

[6] Emanuel Huber and Guillaume Hans. RGPR — an open-source package to process and visualize GPR data. In *2018 17th International Conference on Ground Penetrating Radar (GPR)*, pages 1–4. doi: 10.1109/ICGPR.2018.8441658. URL https://ieeexplore.ieee.org/document/8441658. ISSN: 2474-3844.

[7] J. Wong, Lejia Han, J. Bancroft, and R. Stewart. Automatic time-picking of first arrivals on noisy microseismic data. URL https://www.semanticscholar.org/paper/Automatic-time-picking-of-first-arrivals-on-noisy-Wong-Han/7736aad97bffccf33efe1a5a77e16d7807715c12.

[8] Amir Mardan. geo-stack/first_break_picking. URL https://github.com/geo-stack/first_break_picking. original-date: 2023-07-03T19:03:46Z.

[9] M. Dossi, E. Forte, M. Pipan, R. R. Colucci, and A. Bortoletto. Automated reflection picking and inversion: Application to ground and airborne GPR surveys. In *2016 16th International Conference on Ground Penetrating Radar (GPR)*, pages 1–6. doi: 10.1109/ICGPR.2016.7572640. URL https://ieeexplore.ieee.org/document/7572640.

[10] H. Machguth, O. Eisen, F. Paul, and M. Hoelzle. Strong spatial variability of snow accumulation observed with helicopter-borne GPR on two adjacent alpine glaciers. 33(13). ISSN 1944-8007. doi: 10.1029/2006GL026576. URL https://onlinelibrary.wiley.com/doi/abs/10.1029/2006GL026576. _eprint: https://onlinelibrary.wiley.com/doi/pdf/10.1029/2006GL026576.

[11] Daehyun Kim and Bruce Jamieson. Estimating the density of dry snow layers from hardness, and hardness from density. In *Proceedings of 2014 International Snow Science Workshop, Banff, Canada*. URL https://arc.lib.montana.edu/snow-science/objects/ISSW14_paper_P1.25.pdf.

[12] Zi Xian Leong and Tieyuan Zhu. Direct velocity inversion of ground penetrating radar data using GPRNet. 126(6):e2020JB021047. ISSN 2169-9356. doi: 10.1029/2020JB021047. URL https://onlinelibrary.wiley.com/doi/abs/10.1029/2020JB021047. _eprint: https://onlinelibrary.wiley.com/doi/pdf/10.1029/2020JB021047.

[13] James Irving and Rosemary Knight. Numerical modeling of ground-penetrating radar in 2-d using MATLAB. 32(9):1247–1258. ISSN 0098-3004. doi: 10.1016/j.cageo.2005.11.006. URL https://www.sciencedirect.com/science/article/pii/S0098300405002621.

[14] François Lavoué. 2d full waveform inversion of ground penetrating radar data : towards multiparameter imaging from surface data. URL https://theses.hal.science/tel-01551800.

[15] Martin Chaplin. Water and microwaves. URL https://water.lsbu.ac.uk/water/microwave_water.html.

[16] M. Bavay and T. Egger. MeteoIO 2.4.2: a preprocessing library for meteorological data. 7(6):3135–3151. ISSN 1991-9603. doi: 10.5194/gmd-7-3135-2014. URL https://gmd.copernicus.org/articles/7/3135/2014/.

[17] Regula frf. - 4. mars 2024 15:45+01:00. URL https://regobs.no/registration/385805.

[18] Lubos Mitas and Helena Mitasova. Spatial interpolation. 1(2):481–492. Publisher: Wiley Hoboken, NJ, USA.

ANNEX

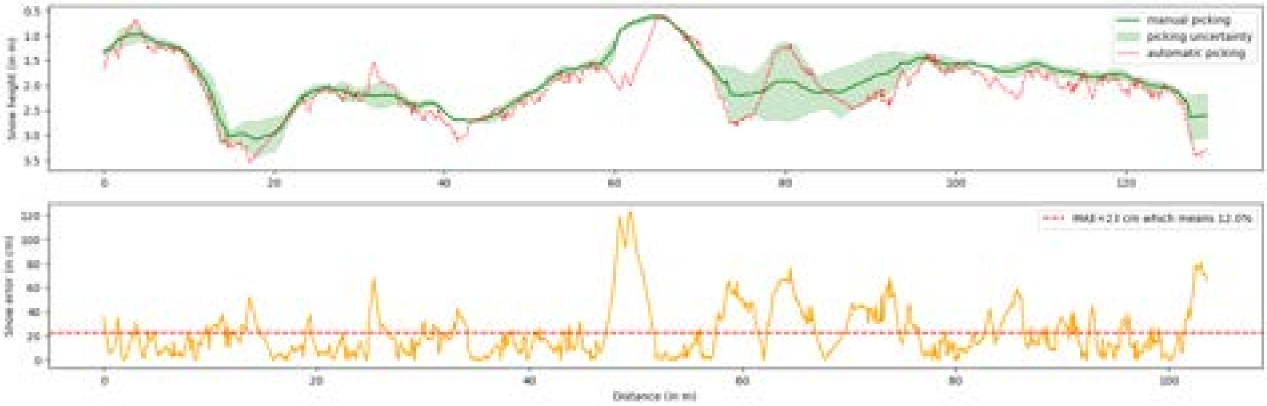

(a) Fonnbu, 2024, rocky field, antenna 1GHz

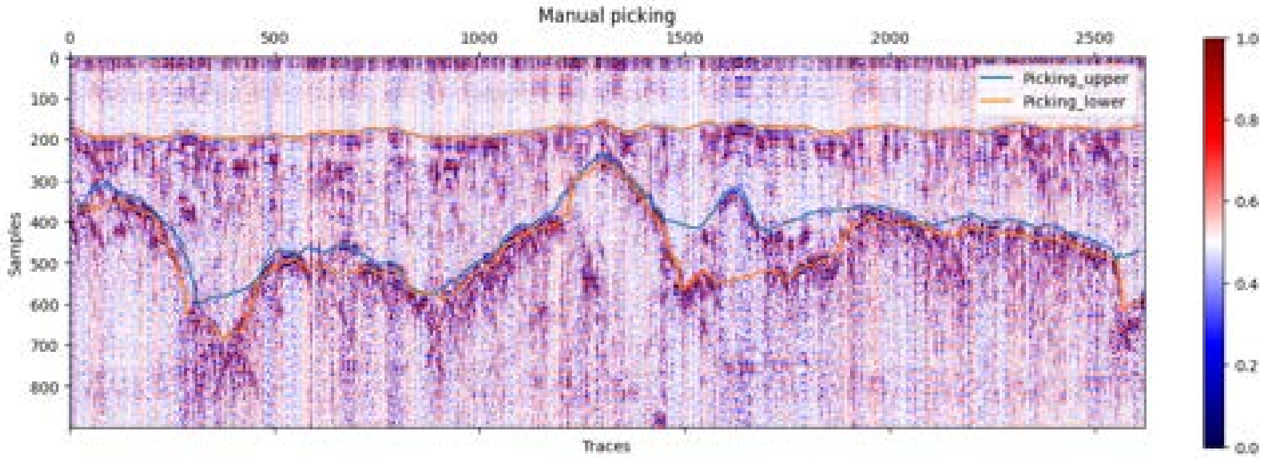

(b) Fonnbu, 2024, GPR profile

Figure 21: Comparison between manual picking and automatic picking in terms of snow height by using an averaged relative permittivity in the snow of $\epsilon_r = 2$

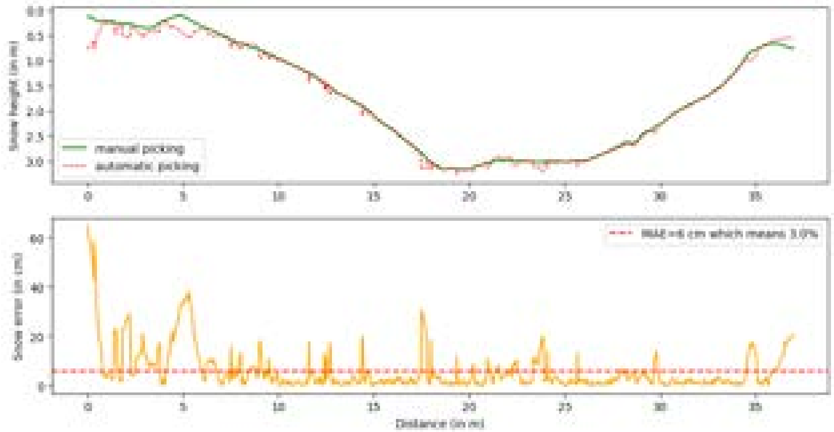

(a) Storlidalen, 2022, homogeneous grassy field in slope(see Figure 8), antenna 1GHz

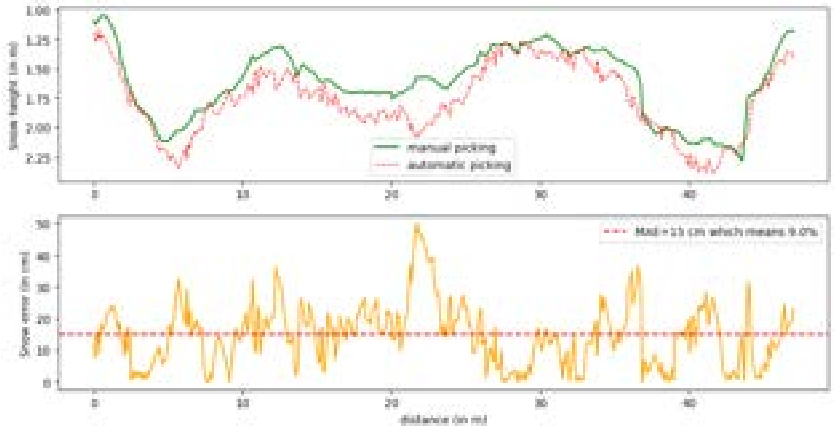

(b) Fonnbu, 2023, heterogeneous rocky field in valley(see Figure 8), antenna 1GHz

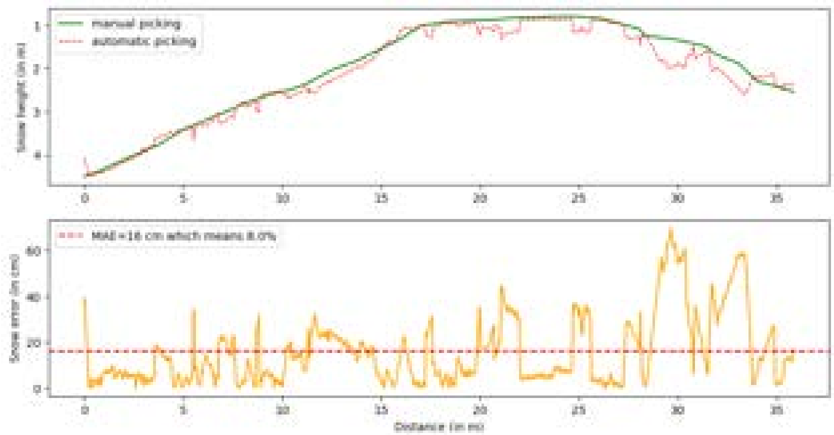

(c) Jufvonne, 2023, homogeneous rocky field in slope(see Figure 8), antenna 400MHz

Figure 22: Comparison between manual picking and automatic picking in terms of(top) snow height and (bottom) absolute snow difference (by using an averaged relative permittivity in the snow of $\epsilon = 2$

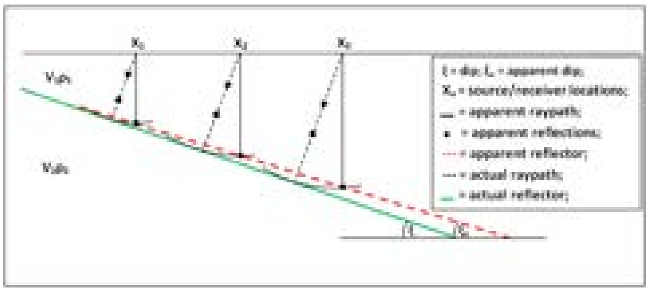

Figure 23: Diagram showing the raypath for a reflection from a dipping reflector and the resultant apparent dip (from wikipedia "Seismic Migration")

Statens vegvesen
Pb. 1010 Nordre Ål
2605 Lillehammer

Tlf: (+47) 22 07 30 00

firmapost@vegvesen.no

ISSN: 1893-1162

vegvesen.no

Tryggere, enklere og grønnere reisehverdag